TESLA Report 2005-15

Far-Infrared Transition and Diffraction Radiation
Part I: Production, Diffraction Effects and Optical Propagation

Sara Casalbuoni[1], Bernhard Schmidt[1] and Peter Schmüser[1,2]

1 Deutsches Elektronen-Synchrotron DESY

2 Institut für Experimentalphysik, Universität Hamburg

1 Introduction

Transition radiation is emitted when a relativistic charged particle crosses the boundary between two media of different dielectric properties. Radiation is also produced if the particle does not cross the discontinuity directly but passes it at such a close distance that its self-field is modified by the sudden change in the dielectric constant. In this case one speaks of diffraction radiation. For a planar boundary of infinite extent, the transition radiation process was calculated analytically by Ginzburg and Frank [1]. In most practical cases, however, the Ginzburg-Frank equation is not applicable because two basic pre-assumptions of the analytic derivation are not fulfilled: the radiation screens used in an accelerator are of limited size, and the radiation is usually observed in the near-field and not in the far-field regime. In this paper, we describe a method which allows to compute the transition or diffraction radiation from a screen of arbitrary shape and size and at any distance from the source. The only condition is that the dimensions of the screen and the distance to the observer must be large compared to the wavelength of the radiation. The method is therefore capable of treating realistic experimental setups.

If the wavelength of the radiation exceeds the electron bunch length, all particles emit their radiation coherently which means that the field amplitudes add with constructive interference and the intensity scales quadratically with the number of electrons per bunch. Coherent transition radiation (CTR) with frequencies in the THz regime is a widely used tool for longitudinal phase space diagnostics of relativistic electron bunches since its spectrum is related to the longitudinal charge profile by Fourier transformation. The radiation has to be coupled out of the vacuum pipe of the accelerator and transported to the detecting device, for example a Martin-Puplett interferometer. Diffraction plays an enormous role in the transport of this rather long-wavelength radiation and has a strong influence on the transfer efficiency as a function of wavelength. The diffraction effects are often quite counter-intuitive, so we have spent considerable time in developing mathematical codes to study them and, wherever possible, in comparing the numerical results to analytical expressions.

The paper is organized as follows. In Section 2 we give a short outline of optical diffraction theory and show that our numerical methods are in perfect agreement with the analytical results for far-field (Fraunhofer) diffraction at a circular aperture, but in addition allow

to compute the near-field (Fresnel) diffraction pictures. Section 3 deals with transition and diffraction radiation of single electrons. An alternative derivation of the well-known Ginzburg-Frank formula is presented, and the formula is generalized to the case of a radiation screen of finite size. A quantitative criterion for the distinction between far-field and near-field diffraction is given. Section 4 is devoted to coherent radiation effects by electron bunches of finite radius and length. In Section 5 we describe a powerful method for the propagation and optical imaging of THz radiation by means of numerical Fourier transformation. The electromagnetic field of relativistic charged particles is derived in Appendix A. The optical properties of focusing mirrors are explained in Appendix B.

2 Basic Elements of Diffraction Theory

2.1 Huygens-Fresnel principle

The starting point of all diffraction phenomena is the Huygens-Fresnel principle which states that each point on a given wave front can be considered as the origin of a secondary spherical wave. All these little wavelets interfere and their envelope forms the new wavefront. Consider first a plane wave

$$E_x(z,t) = E_0 \exp(i(kz - \omega t)) \tag{1}$$

The common phase factor $\exp(-i\omega t)$ is neglected in the following. The wavefront at the plane $z = 0$ has the same electric field amplitude E_0 at each point on this plane. Now consider a point on the z axis at a distance D from this plane. The field at $P = (0, 0, D)$ is according to the Huygens-Fresnel principle

$$E_x(P) = -\frac{ik}{2\pi} \int\int E_0 \frac{e^{ikR}}{R} dxdy \quad \text{with} \quad R = \sqrt{D^2 + x^2 + y^2} \tag{2}$$

We demonstrate now that the factor $-ik/(2\pi) = -i/\lambda$ in front of the integral is needed to get the expected value $E_x(P) = E_0 \exp(i\,kD)$. The integral over the plane $z = 0$ is carried out in cylindrical coordinates:

$$E_x(P) = -\frac{ik}{2\pi}\, E_0 2\pi \int_0^\infty \frac{\exp[(ik-\mu)\sqrt{D^2+r^2}]}{\sqrt{D^2+r^2}}\, r\, dr$$

Here the term $-\mu\sqrt{D^2 + r^2}$ in the exponent has been added to ensure convergence of the integral at the upper limit. Afterwards we take the limit $\mu \to 0$. The integration can be done analytically and yields

$$E_x(P) = \frac{ik}{2\pi}\, E_0 2\pi \frac{\exp[(ik-\mu)D]}{ik-\mu}$$

which for $\mu \to 0$ reduces to $E_x(P) = E_0 \exp(ikD)$, as expected.

Now we consider light from a very distant source that is incident on an opaque screen with an opening, see Fig. 1. We approximate the incident wave by a plane wave of amplitude

A_0 at the screen. The amplitude at an arbitrary point $P = (x, y, D)$ on the other side of the screen is then given by Fresnel-Kirchhoff formula

$$A(P) = -\frac{ik\,A_0}{2\pi} \underbrace{\int\int}_{aperture} \frac{e^{ikR'}}{R'} \frac{\cos\theta_0 + \cos\theta}{2} dS \tag{3}$$

where R' is the distance between P and an arbitrary point inside the opening. The two-dimensional integration must be carried out over the free aperture. This formula is only approximate and requires that the wavelength is much smaller than the radius of the aperture. In this equation an inclination factor

$$\chi = \frac{\cos\theta_0 + \cos\theta}{2} \tag{4}$$

is included which is valid for conventional optical radiation. We will see in Sect. 3 that the inclination factor for transition radiation has a different form.

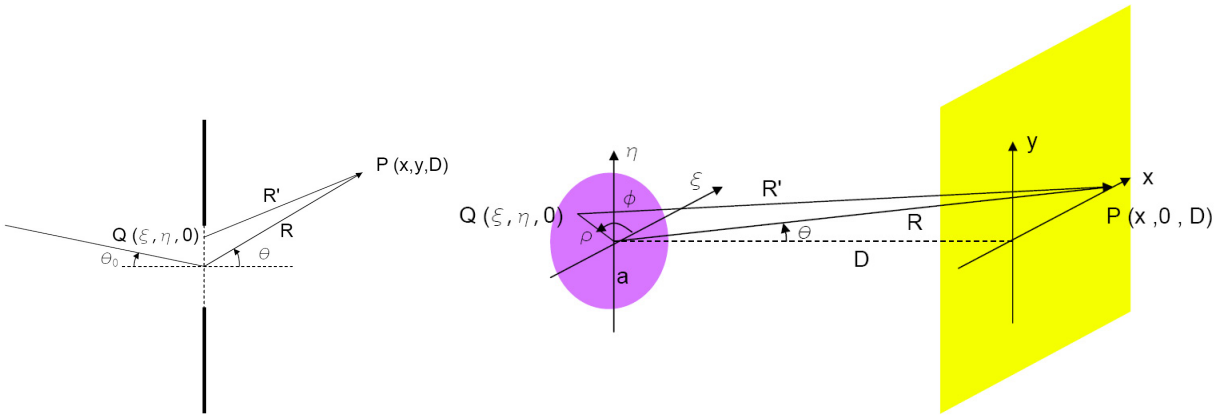

Figure 1: *Diffraction at a circular aperture.*

2.2 Diffraction at a circular aperture

This is a well-known problem in optical diffraction theory which can be solved analytically. We derive first the standard expression for far-field (Fraunhofer) diffraction and present then a method which is capable of describing also the near-field Fresnel diffraction for which an analytical solution does not exist. The source shall be located on the symmetry axis of the aperture and at a very large distance so that the incident light can be treated as a plane wave with an amplitude A_0 at the aperture and an incidence angle $\theta_0 = 0$. Because of the cylindrical symmetry, we can choose the image point to be located on the x axis of the observation screen, $P = (x, 0, D)$. The distance between P and the center of the aperture is

$$R = \sqrt{D^2 + x^2}$$

Let now $Q = (\xi, \eta, 0)$ be an arbitrary point inside the aperture. The distance $R' = \overline{QP}$ is

$$R' = \sqrt{D^2 + (x-\xi)^2 + \eta^2} = \sqrt{R^2 - 2x\xi + \xi^2 + \eta^2} \approx R - \frac{x\rho\cos\phi}{R} + \frac{\rho^2}{2R} \qquad (5)$$

with $\rho = \sqrt{\xi^2 + \eta^2}$ and $\xi = \rho\cos\phi$. The inclination factor χ can be replaced by 1 if we assume that the source is at infinity and $x, y \ll D$. Then the amplitude at P is

$$A(P) = -\frac{ik}{2\pi} A_0 \underbrace{\int\int}_{aperture} \frac{e^{ikR'}}{R'} \, dS$$

where R' is given by Eq. (5). In the denominator of the integrand the distance R' can usually be replaced by R but in the exponent the expression (5) has to be used to get the interference pattern.

2.2.1 Far-field (Fraunhofer) diffraction

Let the image plane be so far away that the quadratic term $\rho^2/(2R)$ in the expansion of R' can be neglected. Then

$$A(P) = -\frac{ik\,A_0}{2\pi} \frac{e^{ikR}}{R} \int_0^a \int_0^{2\pi} \exp(-ik\sin\theta\rho\cos\phi)\, d\phi\, \rho d\rho$$

where we have defined the angle θ by $\sin\theta = x/R$. The angular integration yields the zero-order Bessel function

$$\int_0^{2\pi} \exp(-iu\cos\phi)\, d\phi = 2\pi J_0(u)\,,$$

where $u = \rho k \sin\theta$, so we get

$$A(P) = -\frac{ik\,A_0}{2\pi} \frac{e^{ikR}}{R} \frac{2\pi}{(k\sin\theta)^2} \int_0^{\tilde{a}} J_0(u) u\, du \quad \text{with} \quad \tilde{a} = ak\sin\theta$$

Using

$$\int_0^{\tilde{a}} J_0(u) u du = \tilde{a} J_1(\tilde{a})$$

one obtains for the intensity of the diffraction pattern the well-known expression

$$I(\theta) \propto |f(\theta)|^2 \quad \text{with} \quad f(\theta) = \frac{J_1(ka\sin\theta)}{ka\sin\theta} \qquad (6)$$

2.2.2 Near-field (Fresnel) diffraction

Diffraction in the near-field can be computed by taking the quadratic term $\rho^2/(2R)$ in the Taylor expansion (5) of $R' = \sqrt{R^2 - 2x\xi + \xi^2 + \eta^2}$ into account. The amplitude as a function of the angle θ becomes

$$A(\theta) = -\frac{ik\,A_0}{2\pi} \frac{e^{ikR}}{R} \cdot f(\theta)$$

with

$$f(\theta) = \int_0^a J_0(k\rho \sin\theta)\, \exp\left(ik\frac{\rho^2}{2R}\right) \rho\, d\rho\ . \tag{7}$$

This integral can only be solved numerically. At short distances the resulting angular distribution, shown in Fig. 2, differs considerably from the far-field diffraction pattern.

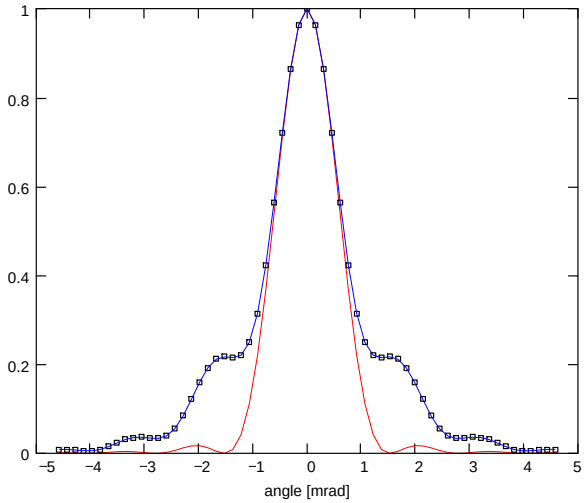

Figure 2: *Diffraction of optical radiation with $\lambda = 500$ nm at a circular aperture of radius $a = 0.2$ mm. Shown is the intensity as a function of the angle θ. Red curve: far-field diffraction pattern, Eq. (6). Blue curve: near-field diffraction pattern according to Eq. (7) at a distance $D = 75$ mm from the aperture. Blue squares: two-dimensional numerical computation using the exact square-root expression (5) for R'. The curves are individually normalized to a maximum value of 1.*

3 Transition and Diffraction Radiation by a Single Electron

In this chapter we deal with the radiation that is emitted when highly relativistic electrons cross the boundary from vacuum to a metal (transition radiation TR) or pass a nearby metallic screen (diffraction radiation DR).

3.1 Ginzburg-Frank formula

Transition radiation was first treated by Ginzburg and Frank by solving the Maxwell equations for a relativistic electron approaching a planar boundary between two media of different dielectric constants. The electromagnetic field carried by the particle changes when going from one medium to the other. To satisfy the boundary conditions for the electric and magnetic field vectors one has to add two radiation fields, propagating in the forward resp. backward direction. For the special case that the electron crosses

the boundary from vacuum to a metallic half plane, only backward radiation is emitted since no radiation can propagate inside the metal. (For a metallic screen with finite thickness, forward radiation is emitted as well). The spectral and spatial radiation energy of backward transition radiation from a single electron is given by the Ginzburg-Frank formula

$$\frac{d^2U}{d\omega d\Omega} = \frac{e^2}{4\pi^3\varepsilon_0 c} \cdot \frac{\beta^2 \sin^2\theta}{(1-\beta^2\cos^2\theta)^2} \tag{8}$$

with $\beta = v/c$ and θ the angle against the backward direction. This formula is only valid in the far-field. For a derivation we refer to Landau-Lifshitz [1]. The angular distribution is shown in Fig. 3. A characteristic feature is the vanishing intensity in the exact backward direction at $\theta = 0$ which is caused by the radial polarization of the radiation.

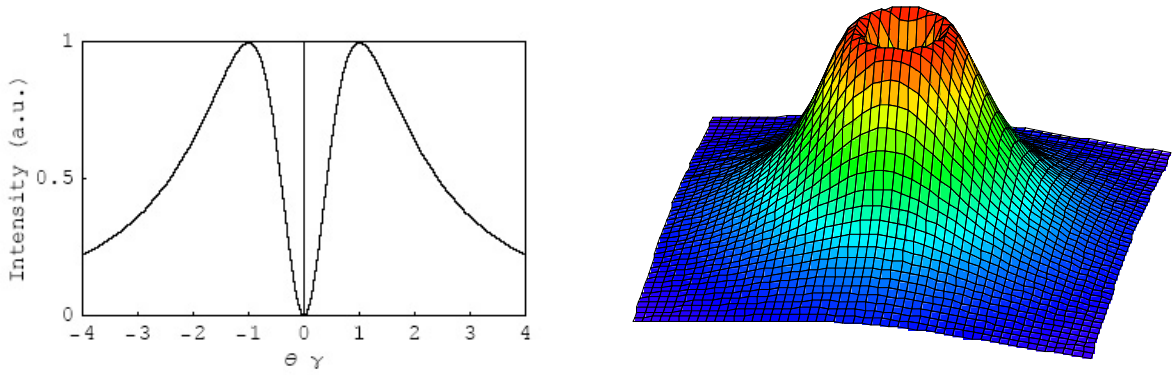

Figure 3: *Angular distribution of the intensity of backward transition radiation according to the Ginzburg-Frank formula.*

The angular distribution has its maximum at the angle

$$\theta_{max} = \arcsin\left(\frac{\sqrt{1-\beta^2}}{\beta}\right) = \arcsin\left(\frac{1}{\beta\gamma}\right) \simeq \frac{1}{\gamma} \quad \text{for} \quad \gamma \gg 1 \tag{9}$$

For $\gamma \gg 1$ (in practice, $\gamma > 10$ is sufficient) the typical angles are small, hence $\sin^2\theta \approx \theta^2$ and $\cos^2\theta \approx 1-\theta^2$. Then the angular dependence simplifies to:

$$\frac{\beta^2\sin^2(\theta)}{\left(1-\beta^2\cos^2(\theta)\right)^2} \approx \frac{\beta^2\theta^2}{\left(1-\beta^2\left(1-\theta^2\right)\right)^2} = \frac{\gamma^2\left(\gamma^2-1\right)\theta^2}{\left(\left(\gamma^2-1\right)\theta^2+1\right)^2} \simeq \gamma^2\frac{(\theta\gamma)^2}{(1+(\theta\gamma)^2)^2} \tag{10}$$

This shows, that the shape of the Ginzburg-Frank distribution is for large γ a universal function of the scaled angle $\theta\gamma$.

For an infinite plane, the spectral transition radiation energy according to Eq. (8) does not depend on frequency, provided one stays well below the plasma frequency of the metal. In the next sections we will see that for a finite TR screen the radiation energy acquires an ω dependence.

3.2 Transition radiation from finite screens

The boundary-condition method can be generalized to describe the radiation from finite screens, but only for very special geometries: circular disk, circular hole in an infinite conducting plane, semi-infinite half plane. This will not be discussed here because the mathematical effort is considerable and the results apply only for far-field diffraction. Radiation from a screen of arbitrary shape cannot be calculated analytically. For this reason, we want to describe now a method which permits the numerical calculation of transition and diffraction radiation from any kind of screen. This method has the additional advantage that it covers not only the far-field (Fraunhofer) diffraction but also the near-field (Fresnel) diffraction. All analytical treatments have the severe drawback that they are only valid in the far-field and are hence rarely applicable to beam diagnostic experiments at accelerators which are mostly done in the near-field regime.

3.2.1 Method of virtual photons

An alternative approach to compute the radiation by a charged particle at the transition from vacuum to a metal is based on the assumption that the *virtual photons*, constituting the self-field of the particle, are converted into *real photons* by reflection at the metallic interface. Effectively this means that the Fourier components of the transverse electric field of the electron are reflected at the metal surface. Then the Huygens-Fresnel principle is applied to compute the outgoing electromagnetic wave. An important prerequisite is the fact that the field of a highly relativistic electron ($\gamma \gg 1$) is concentrated in a flat disk perpendicular to the direction of motion so that the field is essentially transverse[1]. In the following, we want to demonstrate that this alternative treatment reproduces the Ginzburg-Frank angular distribution in case of an infinite metallic screen but leads to entirely new results for finite screens. Moreover, the method is capable of describing both far-field and near-field diffraction.

3.3 Generalization of the Ginzburg-Frank formula

In this section we want to apply the virtual-photon method to compute transition radiation at a circular disk and demonstrate that the Ginzburg-Frank formula results if the disk radius tends to infinity. We study here only the far-field regime because the Ginzburg-Frank formula is not valid in the near-field.

3.3.1 Computation of the field on the observation screen

We take a metallic disk of radius a as our transition radiation (TR) source and use a cylindrical coordinate system $(\rho, \phi, z = 0)$ on the disk. The observation screen is at a distance $D \gg a$ from the TR source. Call $\tilde{E}_r$ the Fourier component of the radial electric field of the incident electron. It will be shown in Appendix A that the Fourier transform of the radial electric field of the electron is given by the modified Bessel function K_1

$$\tilde{E}_r(\rho, \omega) = \frac{-e\omega}{(2\pi)^{3/2}\varepsilon_0\beta^2\gamma c^2}\, K_1\left(\frac{\omega}{\beta\gamma c}\,\rho\right) \tag{11}$$

[1]The virtual-photon method does not appear to be applicable for 'slow' electrons but transition radiation is anyhow unimportant in the non-relativistic regime.

Because of the cylindrical symmetry, the field on the observation screen will be radial as well. Without loss of generality we can therefore choose our target point to be located on the x axis of the observation screen: $P = (x, y = 0, z = D)$. The arrangement is sketched in Fig. 4. The electric field at P will then have only an x component. A small area element at an arbitrary point $Q = (\rho, \phi, 0)$ of the TR source screen at $z = 0$ yields the following contribution to the horizontal field component at P

$$d\tilde{E}_x(P,\omega) = -\frac{ik}{2\pi}\,\tilde{E}_r(\rho,\omega)\cos\phi\,\frac{\exp(ikR')}{R'}\,\rho d\rho d\phi \quad \text{with} \quad k = \frac{\omega}{c}$$

Here $R' = \sqrt{D^2 + (x - \rho\cos\phi)^2 + (\rho\sin\phi)^2}$ is the distance between Q and P. Note that the $1/\rho$ divergence of $\tilde{E}_r(\rho,\omega)$ for $\rho \to 0$ is canceled by multiplication with the area element $\rho\, d\rho d\phi$. The electric field at P is given by integration over the TR source

$$\tilde{E}_x(P,\omega) = -\frac{ik}{2\pi}\int_0^a\int_0^{2\pi}\tilde{E}_r(\rho,\omega)\cos\phi\,\frac{\exp(ikR')}{R'}\,d\phi\rho d\rho\,. \tag{12}$$

Since we restrict ourselves here to the far-field case, the square root is only expanded up to first order in ρ

$$R' = \sqrt{D^2 + (x - \rho\cos\phi)^2 + (\rho\sin\phi)^2} \approx R - \frac{x\rho\cos\phi}{R} \quad \text{with} \quad R = \sqrt{D^2 + x^2} \tag{13}$$

The distance $R' = \overline{QP}$ in the denominator of the integrand of Eq. (12)) can be replaced by the distance R between the center of the TR screen and the observation point P:

$$\frac{\exp(ikR')}{R'} \;\approx\; \frac{\exp(ikR)}{R}\,\exp(-ik\,\rho\sin\theta\cos\phi) \tag{14}$$

As before, we define the angle θ by

$$\sin\theta = x/R$$

Equation (12) can be written as

$$\tilde{E}_x(P,\omega) = -\frac{ik}{2\pi}\,\frac{\exp(ikR)}{R}\int_0^a\int_0^{2\pi}\tilde{E}_r(\rho,\omega)\cos\phi\;\exp(-ik\;\rho\sin\theta\cos\phi)\,d\phi\rho d\rho \tag{15}$$

Inserting $\tilde{E}_r$ from Eq. (11) the field at $P = (x, 0, D)$ becomes

$$\tilde{E}_x(P,\omega) = \frac{iek^2}{(2\pi)^{5/2}\varepsilon_0\beta^2\gamma c}\,\frac{\exp(ikR)}{R}\int_0^a\left[\int_0^{2\pi}K_1\left(\frac{k\rho}{\beta\gamma}\right)\cos\phi\;\exp(-ik\,\rho\sin\theta\cos\phi)\,d\phi\right]\rho d\rho$$

The integration over the azimuthal angle yields the Bessel function J_1

$$\int_0^{2\pi}\exp(-ik\,\rho\sin\theta\cos\phi)\cos\phi d\phi = -2\pi i J_1(k\,\rho\sin\theta)$$

The integration over the radius can be carried out analytically

$$\begin{aligned}\int_0^a J_1(k\rho\sin\theta)K_1\left(\frac{k\rho}{\beta\gamma}\right)\rho d\rho &= \frac{\beta^3\gamma^3\sin\theta}{k^2(1+\beta^2\gamma^2\sin^2\theta)}\,[1 - T(\theta,k)] \\ &= \frac{\beta^3\gamma\sin\theta}{k^2(1-\beta^2\cos^2\theta)}\,[1 - T(\theta,k)] \end{aligned}\tag{16}$$

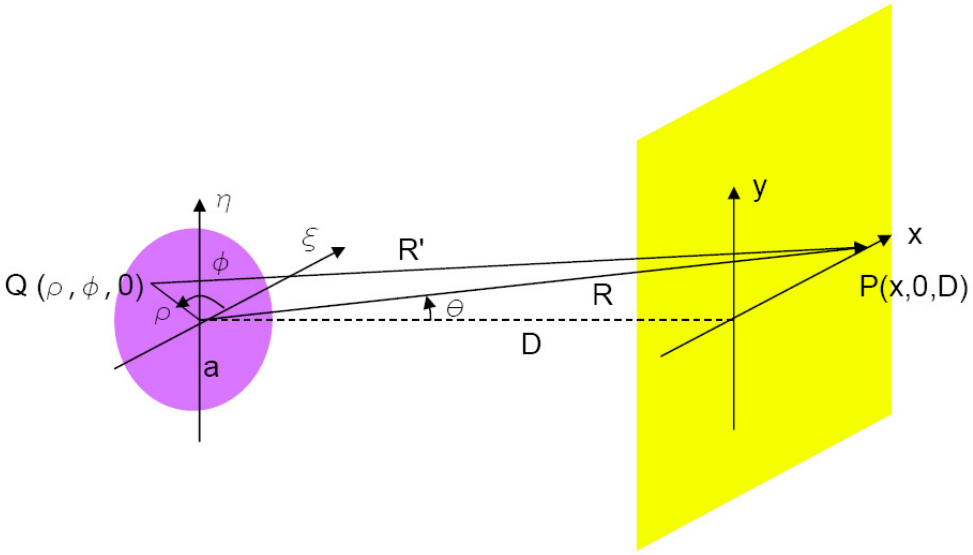

Figure 4: *Diffraction geometry for a finite TR source (metallic screen with radius a) and an observation screen placed at a distance $D \gg a$.*

with

$$T(\theta, k) = \frac{ka}{\beta\gamma} \cdot J_0(ka\sin\theta) K_1\left(\frac{ka}{\beta\gamma}\right) + \frac{ka}{\beta^2\gamma^2\sin\theta} \cdot J_1(ka\sin\theta) K_0\left(\frac{ka}{\beta\gamma}\right) \tag{17}$$

Hence the Fourier-transformed electric field on the observation screen becomes

$$\tilde{E}_x(\theta, \omega) = \frac{e}{(2\pi)^{3/2}\varepsilon_0\, c} \frac{\exp(ikR)}{R} \cdot \frac{\beta\sin\theta}{1-\beta^2\cos^2\theta}\,[1 - T(\theta, k)] \tag{18}$$

3.3.2 Radiated energy

In order to understand how the radiated energy per frequency interval is calculated from the Fourier components we first look at the simpler case of an electromagnetic wave pulse traveling in z direction, but without a dependence on x and y. This pulse can be expressed as a superposition of plane waves

$$E_x(z,t) = \frac{1}{\sqrt{2\pi}} \int_{-\infty}^{\infty} \tilde{E}(\omega) \exp[i\omega(z/c - t)] d\omega = \frac{2}{\sqrt{2\pi}} \int_0^{+\infty} \tilde{E}(\omega) \exp[i\omega(z/c - t)] d\omega$$

The Fourier components of the magnetic field are given by

$$\tilde{B}(\omega) = \tilde{E}(\omega)/c$$

The energy flow is given by the Poynting vector, which for complex fields is written as

$$\boldsymbol{S} = \frac{1}{2\mu_0} \boldsymbol{E} \times \boldsymbol{B}^* \qquad S_z = \frac{1}{2\mu_0} E_x B_y^*$$

The total energy per unit area, flowing through the detector plane at $z = 0$, is

$$U_{tot} = \int_{-\infty}^{\infty} dt\, S_z(0,t) = \frac{1}{2\mu_0} \int_{-\infty}^{\infty} dt \left[E_x(0,t) B_y^*(0,t) \right]$$

In terms of the Fourier components the energy flow is

$$U_{tot} = \frac{1}{\pi\mu_0} \int_0^{\infty} d\omega \int_0^{\infty} d\omega' \tilde{E}(\omega)\tilde{B}^*(\omega') \int_{-\infty}^{\infty} dt \left[\exp(-i(\omega - \omega')t) \right]$$

The time integration yields $2\pi\delta(\omega - \omega')$, hence

$$U_{tot} = \frac{2}{\mu_0 c} \int_0^{\infty} d\omega \left| \tilde{E}(\omega) \right|^2$$

Writing

$$U_{tot} = \int_0^{\infty} \frac{dU}{d\omega}\, d\omega$$

we get for the spectral energy density

$$\frac{dU}{d\omega} = \frac{2}{\mu_0 c} \left| \tilde{E}(\omega) \right|^2 = 2\,\varepsilon_0\, c \left| \tilde{E}(\omega) \right|^2 \tag{19}$$

3.3.3 Generalized Ginzburg-Frank formula

In transition radiation, the field depends not only on frequency but also on the transverse coordinates x, y, or alternatively on the deflection angle θ. Putting (18) into Eq. (19) and keeping in mind that the area element dS at the point P on the observation screen is $dS = R^2 d\Omega$, we obtain for the spectral energy as a function of the angle θ

$$\boxed{\frac{d^2U}{d\omega d\Omega} = \frac{e^2}{4\pi^3 \varepsilon_0\, c} \cdot \frac{\beta^2 \sin^2\theta}{(1 - \beta^2\cos^2\theta)^2} \left[1 - T(\theta,\omega)\right]^2} \tag{20}$$

with

$$T(\theta,\omega) = \frac{\omega a}{c\beta\gamma} J_0\left(\frac{\omega a \sin\theta}{c}\right) K_1\left(\frac{\omega a}{c\beta\gamma}\right) + \frac{\omega a}{c\beta^2\gamma^2 \sin\theta} J_1\left(\frac{\omega a \sin\theta}{c}\right) K_0\left(\frac{\omega a}{c\beta\gamma}\right) \tag{21}$$

Equation (20) is the generalization of the Ginzburg-Frank formula for a TR source of finite radius a. The correction term (17) has been written here as a function of θ and $\omega = k\, c$. This form is found in the literature [2].
Formula (20) reveals a frequency dependence of the radiated energy. The term $T(\theta,\omega)$ depends on the product $\omega a \propto a/\lambda$. This means that the angular distribution remains invariant if the disk radius a and the wavelength λ of the TR are scaled by the same factor. Note that the generalized Ginzburg-Frank formula is only valid in the far-field regime because in the derivation we have used the first-order expansion of the distance R'.

3.3.4 Limits of infinite resp. vanishing source size

In the case of a large TR source, i.e. in the limit $a \to \infty$, we expect to recover the Ginzburg-Frank equation. This is indeed the case. For a large source radius the term $T(\theta, \omega)$ tends to zero:

$$\lim_{a\to\infty} a\, J_0\left(\frac{\omega a \sin\theta}{c}\right) K_1\left(\frac{\omega a}{c\beta\gamma}\right) = 0$$
$$\lim_{a\to\infty} a\, J_1\left(\frac{\omega a \sin\theta}{c}\right) K_0\left(\frac{\omega a}{c\beta\gamma}\right) = 0$$

Therefore we obtain for the spectral energy density

$$\boxed{\frac{d^2U_{GF}}{d\omega d\Omega} = \frac{e^2}{4\pi^3\varepsilon_0\, c} \cdot \frac{\beta^2 \sin^2\theta}{(1-\beta^2\cos^2\theta)^2}} \tag{22}$$

This completes the proof that for a "large" TR source, and in the far-field, our virtual-photon method reproduces the classical Ginzburg-Frank formula.

On the other hand, for an infinitesimally small TR source the radiation energy should be zero. Also this limit is correctly reproduced by formula (20) since

$$\lim_{a\to 0} T(\theta, \omega) = 1$$

3.4 Validity range of the Ginzburg-Frank formula, extension to the near-field

In this section we study numerically the generation of transition radiation at a source with the shape of a circular disk. For each Fourier component, the outgoing waves are propagated to an observation plane at a distance D which is large compared to the wavelength of the radiation and also large compared to the radius a of the disk. We have seen in Sect. 3.3 that the Ginzburg-Frank angular distribution is obtained if (i) the TR screen size is big enough and (ii) the observation screen is at a sufficiently large distance from the source. These conditions will now be quantified.

3.4.1 Second-order calculation

In order to cover the near-field we now expand the distance R' between an arbitrary source point $Q = (\rho, \phi, 0)$ and the observation point $P = (x, 0, D)$ up to the second order in the small quantity $\rho/R \ll 1$ where $R = \sqrt{D^2 + x^2}$ is the distance between the center of the TR source and the observation point P. (Note that $x/R = \sin\theta$ is usually also much smaller than 1).

$$R' = \sqrt{D^2 + (x - \rho\cos\phi)^2 + (\rho\sin\phi)^2} \;\approx\; R - \frac{x\rho\cos\phi}{R} + \frac{\rho^2}{2R} \tag{23}$$

The second term is responsible for far-field diffraction. If in addition the third term is taken into account, one can also describe the near-field diffraction pattern. The electric

field at $P = (x, 0, D)$ is in second order in ρ

$$\tilde{E}_x(P,\omega) \propto \int_0^a \left[\int_0^{2\pi} K_1\left(\frac{k\rho}{\beta\gamma}\right) \cos\phi \;\; \exp(-ik\,\rho\,\sin\theta\cos\phi) \exp\left(ik\frac{\rho^2}{2R}\right) \, d\phi \right] \rho d\rho \quad (24)$$

The integration over the azimuthal angle can be carried out as before, yielding $J_1(k\rho\sin\theta)$. The angular dependence of the intensity is therefore in second order

$$\frac{d^2U^{(2)}}{d\omega d\Omega} \propto \left| \int_0^a J_1(k\rho\sin\theta) K_1\left(\frac{k\rho}{\beta\gamma}\right) \exp\left(ik\frac{\rho^2}{2R}\right) \rho\, d\rho \right|^2 \quad (25)$$

The integral (25) can only be solved numerically.
The first-order angular distribution has already been derived in Sect. 3.3, we quote the result for completeness

$$\frac{d^2U^{(1)}}{d\omega d\Omega} \propto \left| \int_0^a J_1(k\rho\sin\theta) K_1\left(\frac{k\rho}{\beta\gamma}\right) \rho\, d\rho \right|^2 \quad (26)$$

Here the integration can be done analytically and yields the generalized Ginzburg-Frank formula (20). Note the similarity between the two integrals, in order to describe the diffraction effects at small distance it is sufficient to include the additional phase factor $\exp(ik\rho^2/(2R))$. This fact will be used in the numerical computation of diffraction patterns by Fourier transformation in Sect. 5.

3.4.2 Effective source radius and far-field condition

When the disk radius a is very large and the observation screen sufficiently far away the Ginzburg-Frank angular distribution is obtained. The question is, how large the radius has to be. It turns out that the answer depends on the wavelength and the Lorentz factor. Following Castellano et al. [2] we define an *effective source radius* by

$$r_{eff} = \gamma\lambda \quad (27)$$

The first condition for obtaining the Ginzburg-Frank angular distribution is that the TR screen radius has to exceed the effective source radius

$$\boxed{r_{screen} \equiv a \geq r_{eff} = \gamma\lambda} \quad (28)$$

In fact, when this condition is fulfilled the term $T(\theta,\omega)$ in the generalized Ginzburg-Frank formula (20) is much smaller than 1. If however the screen radius a is well below the effective source radius, the correction term $T(\theta,\omega)$ becomes significant, see Fig. 5.

The condition for far-field diffraction can be written as

$$\boxed{D > \gamma\, r_{eff} = \gamma^2\lambda} \quad (29)$$

This latter condition can be understood by looking at the Fresnel zone construction in light optics. The radius of the n^{th} Fresnel zone is given by $r_n = \sqrt{n\,\lambda\,D}$. The far-field is safely reached when only the first Fresnel zone contributes, i.e. when

$$r_1^2 > r_{eff}^2 \quad \Rightarrow \quad D > \gamma^2\lambda$$

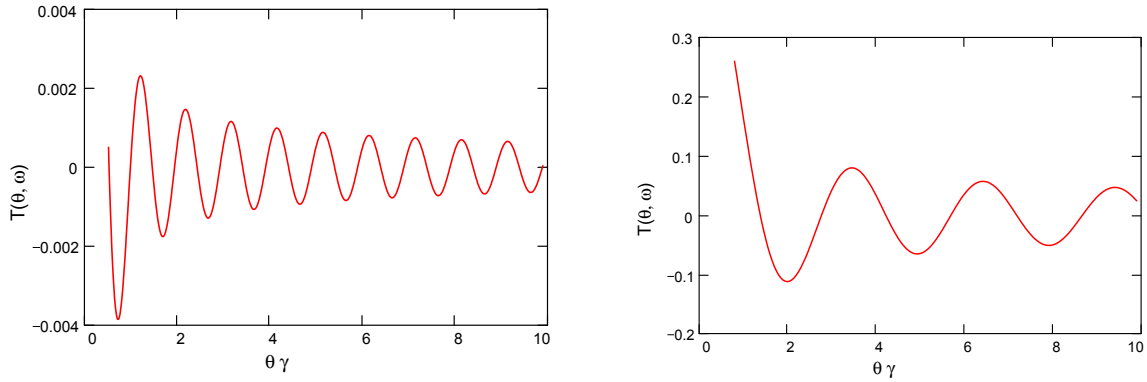

Figure 5: *The term $T(\theta, \omega)$ in the generalized Ginzburg-Frank formula (20), plotted as a function of $\theta\gamma$. Parameters: frequency $f = 1$ THz, TR screen radius $a = 30$ mm.*
Left plot: $\gamma = 100$, $a/r_{eff} = 1$, the effective source size condition (28) is fulfilled. $|T(\theta, \omega)|$ is less than 0.1%.
Right plot: $\gamma = 300$, $a/r_{eff} = 0.33$, the effective source size condition (28) is violated. $|T(\theta, \omega)|$ exceeds 20%.

Far-field, influence of source radius. First we look at the source-radius condition in the far-field. Figure 6 illustrates condition (28) for $\lambda = 0.3$ mm, $\gamma = 100$ and $r_{eff} = 30$ mm. The far-field condition requires then $D > 3$ m, we choose $D = 4$ m. One can see from the figure that for a source radius $a \geq r_{eff}$ the second-order formula (25) is in good agreement with the Ginzburg-Frank formula (the same is of course true for the first-order formula (26)). However, for a very small source radius, e.g. $a = 0.1 \cdot r_{eff}$, the angular distribution becomes much wider than predicted by Ginzburg-Frank. It is interesting to note that in the far-field regime the first-order equation (26) and the second-order equation (25) yield the same result but both differ considerably from the Ginzburg-Frank distribution if condition (28) is violated.

Near-field diffraction. For our previous parameters $\lambda = 0.3$ mm and $\gamma = 100$ the source-radius condition implies $a \geq 30$ mm, we choose $a = 30$ mm. Now we consider the extreme near-field case and choose $D = 0.2$ m, hence $D \ll \gamma^2\lambda = 3$ m. In Fig. 7 the first-order and second-order angular distributions are compared to the Ginzburg-Frank angular distribution. The first-order equation (26) is in perfect agreement with the Ginzburg-Frank formula while in second order we get a significantly wider distribution. This is clear evidence for a near-field effect.

An important result of our investigations is that there is no need to go to even higher orders in the Taylor expansion of R'. The results obtained with the second-order formula (25) are, for all cases considered, in perfect agreement with a two-dimensional numerical computation based on the exact square-root expression (23) for the distance R'.

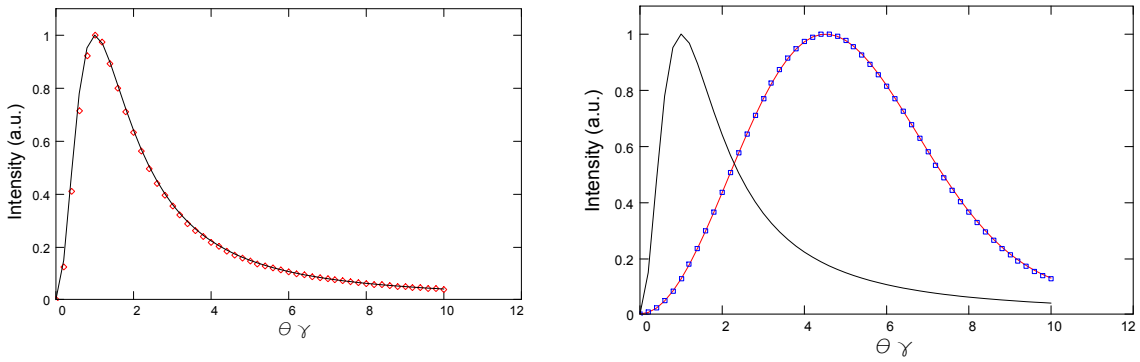

Figure 6: *Far-field transition radiation from a circular disk for $\lambda = 0.3$ mm, $\gamma = 100$, $r_{eff} = 30$ mm, $D = 4$ m. The far-field condition (29) is satified: $D > \gamma\, r_{eff} = 3$ m.*
Left plot: $a = r_{eff} = 30$ mm, the source size condition (28) is fulfilled. The Ginzburg-Frank distribution (black curve) agrees with the second-order computation using Eq. (25), shown by the red diamonds.
Right plot: $a = 0.1 \cdot r_{eff} = 3$ mm, the source size condition (28) is strongly violated. Black curve: Ginzburg-Frank formula; blue squares: first order computation using Eq. (26); red curve: numerical calculation using the exact square root expression for R'. The distributions are individually normalized to a maximum value of 1.

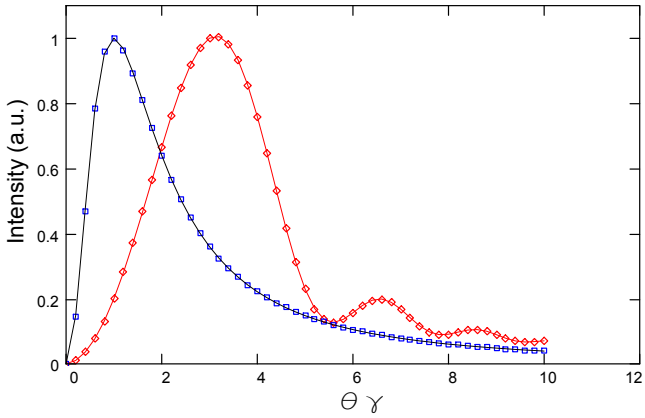

Figure 7: *Near-field transition radiation from a circular disk for $\lambda = 0.3$ mm, $\gamma = 100$, $a = r_{eff} = 30$ mm, $D = 0.2$ m. The effective source size condition (28) is fulfilled but the far-field condition (29) is badly violated. Black curve: Ginzburg-Frank formula; blue squares: first-order computation using Eq. (26); red curve: second-order calculation using Eq. (25); red diamonds: numerical calculation using the exact square root expression for R'.*

3.4.3 Application to the VUV-FEL

The coherent transition radiation (CTR) at the VUV-FEL linac ranges from about 100 GHz to 30 THz. For a typical frequency of 1 THz, corresponding to a wavelength of 0.3 mm, and a Lorentz factor of 1000 ($E_e \approx 500$ MeV), the effective TR source radius is then in the order of 300 mm and exceeds the actual radius a of the TR screen by more

than an order of magnitude. Moreover, the typical distance from the TR source to the first mirror of an interferometer is about 250 mm. Hence, both conditions ($a \geq r_{eff}$ and $D > \gamma^2\lambda$) are strongly violated and the resulting TR angular distribution will be much wider than the Ginzburg-Frank distribution, an example is shown in Fig. 8. For these reasons numerical methods are indispensible for calculating the CTR radiation characteristics. Obviously the near-field calculation based on the second-order formula (25) is needed

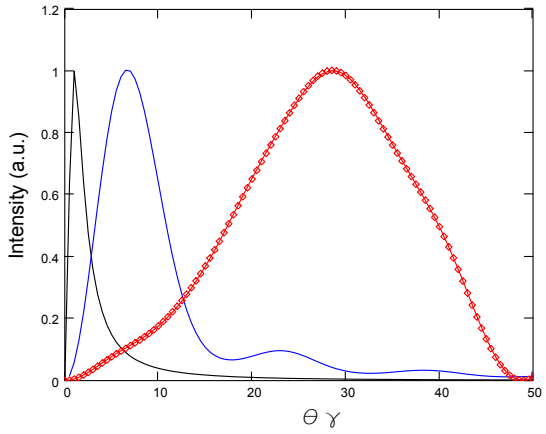

Figure 8: *Typical angular distribution of transition radiation at the VUV-FEL. Parameters:* $\lambda = 0.3$ *mm,* $\gamma = 1000$, $a = 20$ *mm,* $D = 250$ *mm. Black curve: Ginzburg-Frank formula; blue curve: far-field computation using the first-order Eq. (26); red curve: near-field computation using the second-order Eq. (25); red diamonds: near-field calculation using Eq. (12) with the exact square root expression for* R'.

to obtain the correct angular distribution. As mentioned above, this approximation is sufficient for all practical cases, using instead the exact square-root expression for the distance R' between source point Q and image point P yields only marginal changes.

3.5 Total radiated energy

The total spectral energy radiated by an electron that crosses the boundary from vacuum to an infinite metallic plane is obtained by integrating Eq. (8) over the backward hemisphere.

$$\frac{dU}{d\omega} = 2\pi \int_0^{\pi/2} \frac{d^2U}{d\omega d\Omega} \sin\theta \, d\theta = \frac{e^2\beta^2}{2\pi^2\varepsilon_0 c} \int_0^1 \frac{1-u^2}{(1-\beta^2u^2)^2} \, du$$

with $u = \cos\theta$. The integration can be done analytically and yields for the energy per ω interval, radiated by one electron

$$\frac{dU}{d\omega} = \frac{e^2}{8\pi^2\varepsilon_0 c} \cdot \left(\frac{1+\beta^2}{\beta} \ln\left(\frac{1+\beta}{1-\beta}\right) - 2 \right) \approx \frac{e^2}{2\pi^2\varepsilon_0 c} \cdot (\ln\gamma + \ln 2 - 0.5) \qquad (30)$$

Here the last expression results from a first-order Taylor expansion in $1/\gamma$. We get the remarkable result that for an infinite metallic plane the radiated energy is independent of the angular frequency $\omega = 2\pi f$. This, however, does not imply that the energy loss

of the particle diverges if one integrates over all frequencies. In fact, the Ginzburg-Frank formula holds only up to optical frequencies and breaks down when the plasma frequency of the metal is approached which is in the ultraviolet for most metals. Here the refractive index is no longer constant, as assumed in the derivation of the Ginzburg-Frank formula, but exhibits a resonance structure. Integrating over all wavelengths above 100 nm yields a rather modest energy loss of about 0.4 eV when a relativistic electron with $\gamma = 1000$ crosses the interface between vacuum and a metal. Notice, that due to coherent transition radiation effects, the energy loss per electron can become quite substantial if a bunch with high charge crosses the interface between two media (see Sect. 4).

We have seen in the previous section that for a finite TR screen the radiation energy acquires an ω dependence. The spectral energy density $d^2U/(d\omega d\Omega)$, given by the generalized Ginzburg-Frank formula (20), can no longer be integrated analytically over the solid angle, so the total radiated energy must be computed by numerical integration. In Fig. 9, the TR energy per frequency interval $\Delta f = 1$ GHz, that is emitted by an electron with $\gamma = 1000$, is plotted as a function of the TR screen radius a. The wavelength is varied between 100 μm and 3 mm. All curves show a rise with increasing TR screen radius. For $\lambda = 100$ μm the asymptotic value of the radiated energy, as given by Eq. (30), is reached at a screen radius $a > 20$ mm.
Figure 10 shows the TR energy as a function of frequency for a fixed screen radius of $a =$ 20 mm. The low frequencies (large wavelengths) are suppressed because here the effective source size condition (27) is badly violated. The $\gamma = 1000$ curve reaches its intensity plateau later than the $\gamma = 100$ curve since the effective source size $r_{eff} = \gamma\lambda = \gamma c/f$ is a factor of ten larger. From our numerical studies we infer that the condition on the TR screen size for reaching the plateau in the integrated intensity is relaxed as compared to that derived from the angular distribution (Sect. 3.4): we find that $a \geq r_{eff}/3$ is sufficient. Although in the range $r_{eff}/3 < a < r_{eff}$ the angular distribution is wider than the Ginzburg-Frank distribution the total intensity is still the same.

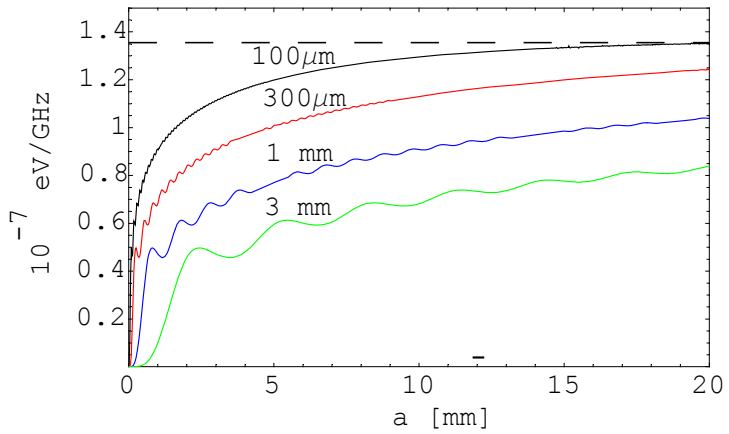

Figure 9: *Transition radiation by single electrons. The TR energy in eV per GHz bandwidth is shown as a function of the TR screen radius a for wavelengths from* 100 μm *to 3 mm. Lorentz factor* $\gamma = 1000$. *The asymptotic limit given by formula (30) is shown as a dashed line.*

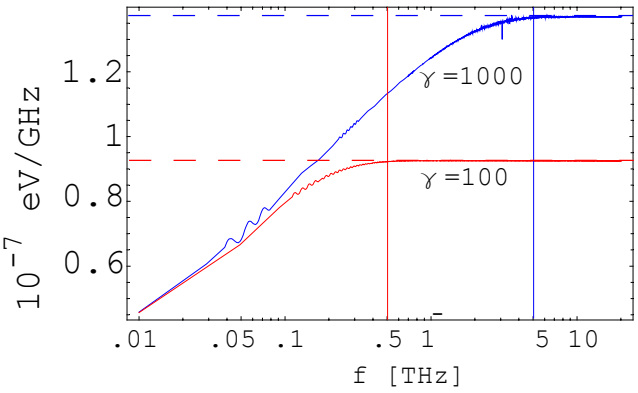

Figure 10: *Single-electron TR energy in eV per GHz as a function of frequency for a fixed TR screen radius $a = 20$ mm. Blue curve: $\gamma = 1000$, red curve: $\gamma = 100$. The blue and red vertical lines indicate the respective frequencies above which the relaxed effective source size condition $a \geq r_{eff}/3$ is fulfilled. The asymptotic limits (30) are shown as horizontal dashed lines.*

3.6 Diffraction Radiation

Diffraction radiation (DR) is produced when relativistic electrons pass a near-by metallic screen. Since the screen does not intercept the particle beam the undesirable side effects of transition radiators, such as emittance growth due to multiple scattering in the material or the destruction of the radiator by a long train of bunches, are avoided. Wake fields are of course still present and may reduce the beam quality somewhat.
We choose as our DR screen a circular disk with radius a which has a central hole of radius b. The spectral energy as a function of the deflection angle can be derived in complete analogy with the treatment in Sect. 3.3. We obtain

$$\begin{aligned}
\frac{d^2U}{d\omega d\Omega} &= \frac{d^2U_{GF}}{d\omega d\Omega} \cdot [T_b(\theta,\omega) - T_a(\theta,\omega)]^2 \qquad (31)\\
T_a(\theta,\omega) &= \frac{\omega a}{c\beta\gamma} J_0\left(\frac{\omega a \sin\theta}{c}\right) K_1\left(\frac{\omega a}{c\beta\gamma}\right) + \frac{\omega a}{c\beta^2\gamma^2 \sin\theta} J_1\left(\frac{\omega a \sin\theta}{c}\right) K_0\left(\frac{\omega a}{c\beta\gamma}\right)\\
T_b(\theta,\omega) &= \frac{\omega b}{c\beta\gamma} J_0\left(\frac{\omega b \sin\theta}{c}\right) K_1\left(\frac{\omega b}{c\beta\gamma}\right) + \frac{\omega b}{c\beta^2\gamma^2 \sin\theta} J_1\left(\frac{\omega b \sin\theta}{c}\right) K_0\left(\frac{\omega b}{c\beta\gamma}\right)
\end{aligned}$$

The case of an infinite DR screen with a hole of radius b is obtained by taking the limit $a \to \infty \quad \Rightarrow\ T_a(\theta,\omega) \to 0$. On the other hand, for a finite screen with a very small hole ($b \to 0 \quad \Rightarrow\ T_b(\theta,\omega) \to 1$) we recover the generalized Ginzburg-Frank formula (20).
In Fig. 11 we compare the far-field angular distribution of TR, produced at a disk with radius $a = 20$ mm, with that of DR at the same-size disk but with a central hole of radius $b = 2$ mm. The distributions are all normalized to the Ginzburg-Frank formula. For a relativistic γ factor of 1000 (left picture) we observe a clear reduction of the radiated intensity with increasing frequency (10 to 30 THz). This loss is much more pronounced at $\gamma = 500$, here the very high frequencies are strongly suppressed. It is interesting to note that the central hole leads at high frequency to an angular distribution which is narrower than the Ginzburg-Frank distribution.

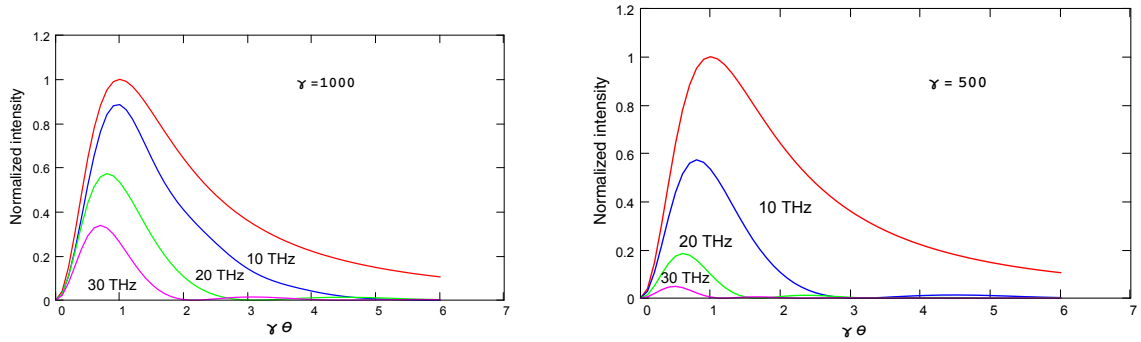

Figure 11: *Angular distribution of transition and diffraction radiation on a circular disk (radius $a = 20$ mm). Red curve: TR on a disk without hole, the other curves refer to DR on a disk of radius $a = 20$ mm which has a central hole of radius $b = 2$ mm. Blue curve: 10 THz, green curve 20 THz, violet curve 30 THz. Left picture: $\gamma = 1000$, right picture: $\gamma = 500$.*

Formula (31) can only be integrated numerically over the solid angle to obtain the total spectral energy. Typical results are shown in Fig. 12. The integrated DR spectral energy is plotted as a function of frequency for DR screens with a central hole of radius $b = 2$ mm. The main effect of the hole is a strong suppression of the high frequency components, which is more pronounced at $\gamma = 100$ than at $\gamma = 1000$. This example explains why diffraction radiation will not extend into the optical regime. The unfortunate consequence is that optical imaging of an electron beam requires a screen that intercepts the beam. If the DR screen has a limited size one observes in addition a reduction of the intensity at low frequencies. The frequency spectrum is then more uniform, which is an advantage for spectroscopy.

3.7 Inclination factor

In this section we show that the inclination factor of transition radiation is simply

$$\chi = \cos\theta \tag{32}$$

where as before θ is the angle between the outgoing radiation, as seen by the observer, and the normal of the TR source screen. To understand this we follow a different approach to compute TR, suggested by D. Suetterlin [3]. The time-varying azimuthal magnetic field of the electron induces radial currents in the metallic source screen. The vector potential generated by these currents is

$$\boldsymbol{A}(\boldsymbol{r},t) = \frac{\mu_0}{4\pi}\int \frac{\boldsymbol{j}(\boldsymbol{r'},t-|\boldsymbol{r}-\boldsymbol{r'}|/c)}{|\boldsymbol{r}-\boldsymbol{r'}|}\,d^3r'$$

This formula shows that the vector $\boldsymbol{A}$ is parallel to the current density $\boldsymbol{j}$ which flows along the surface of the source screen. Now we look at the radiation that propagates at angle θ with respect to the normal vector $\boldsymbol{n}$ of the TR screen, see Fig. 13a. Then one has to project out the component $A_\perp = |\boldsymbol{A}|\cos\theta$ which is perpendicular to the wave vector $\boldsymbol{k}$ since the electric field $\boldsymbol{E} = -\partial\boldsymbol{A}/\partial t$ of the outgoing wave must be transverse.

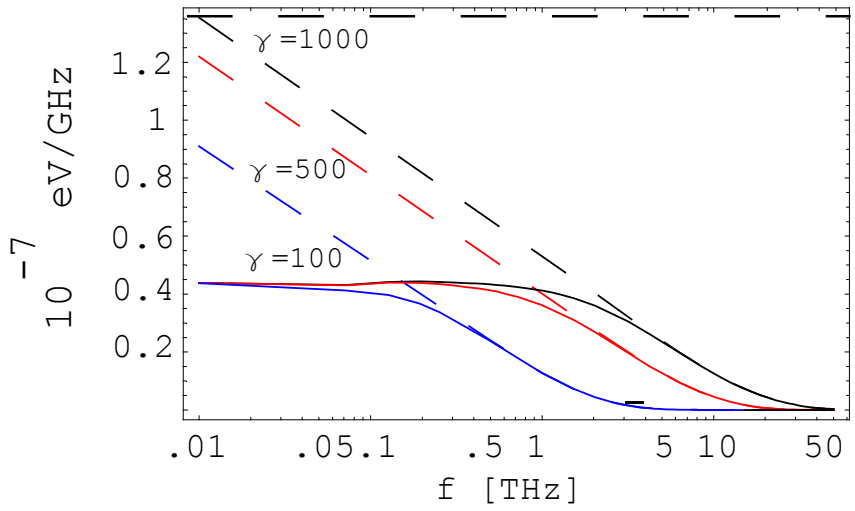

Figure 12: *Integrated DR spectral energy per electron as a function of frequency for DR screens with a central hole of radius $b = 2$ mm. Blue curves: $\gamma = 100$, red curves: $\gamma = 500$, black curves: $\gamma = 1000$. The dashed curves refer to an infinite DR screen, the solid curves to a finite DR screen with an outer radius $a = 20$ mm.*

The inclination factor is close to unity for backward transition radiation since the typical angles θ are small. For beam diagnostics, however, the TR screen is inclined by 45° with respect to the electron beam axis to couple the radiation out of the beam pipe. In this case the inclination factor destroys the azimuthal symmetry of the TR intensity around the outgoing direction. Projected into the 90° deflection plane we obtain a left-right asymmetry in the TR intensity. Figure 13b shows the result of a numerical computation for $\gamma = 1000$, a TR screen radius $a = 12.5$ mm and a wavelength $\lambda = 600$ μm.

4 Coherent Transition Radiation by an Electron Bunch

In Section 3 we have studied the radiation emitted by single electrons. When the radiation wavelength is much shorter than the electron bunch dimensions all electrons radiate incoherently and the TR intensity scales linearly with the number of electrons per bunch:

$$I_N = N I_1$$

This is usually the case in the optical regime, so OTR (optical transition radiation) is predominantly incoherent. In the Terahertz regime, however, the radiation wavelength becomes comparable to the transverse and longitudinal bunch size. Then many particles emit their radiation coherently which means that the amplitudes add with constructive interference. Hence the coherent transition radiation (CTR) intensity grows quadratically with the number N of electrons in the bunch. The relative amount of coherent respectively incoherent transition radiation at a given wavelength depends obviously on the length and radius of the electron bunch.

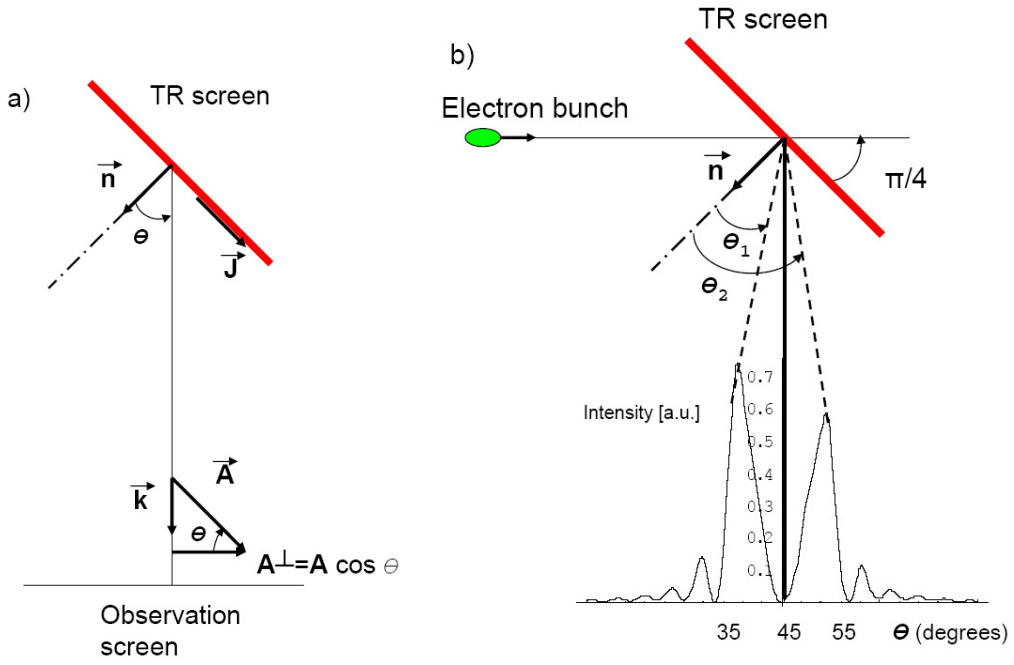

Figure 13: *(a) The inclination angle θ between the wave vector $\boldsymbol{k}$ of the outgoing radiation and the normal vector $\boldsymbol{n}$ of the TR screen. (b) The inclination factor $\chi = \cos\theta$ induces a left-right asymmetry in the TR intensity.*

In the first step we neglect the bunch length and consider a very simple transverse charge distribution, namely a cylindrical electron bunch of radius r_b with homogeneous charge density. The Fourier-transformed radial electric field of such an inifinitely short bunch is (see Appendix A)

$$\tilde{E}_r(\rho,\omega) = \frac{-2eN}{(2\pi)^{3/2} c\beta\varepsilon_0 r_b} \cdot \begin{cases} K_1\left(\frac{\omega}{c\beta\gamma} r_b\right) I_1\left(\frac{\omega}{c\beta\gamma}\rho\right) & \text{for} \quad \rho < r_b \\ I_1\left(\frac{\omega}{c\beta\gamma} r_b\right) K_1\left(\frac{\omega}{c\beta\gamma}\rho\right) & \text{for} \quad \rho > r_b \end{cases} \tag{33}$$

In the second step we admit a finite bunch length. When this bunch traverses the TR screen, it appears to the observer as a very short time-pulse which can be characterized by a longitudinal particle density distribution $\rho_{long}(t)$ which we normalize to unity

$$\int_{-\infty}^{+\infty} \rho_{long}(t)\, dt = 1$$

The particle density in the bunch is $N \cdot \rho_{long}(t)$. We subdivide the bunch into thin slices. Electrons in different slices arrive at the TR screen at different times. Therefore their transition radiation acquires a phase factor $\exp(-i\omega t)$ relative to the radiation emitted by an electron at the center of the distribution (at $t = 0$). As a consequence, the radial electric field of the bunch is given by the product

$$\tilde{E}_r(\rho,\omega) \cdot \int_{-\infty}^{+\infty} \rho_{long}(t) \exp(-i\omega t)\, dt \tag{34}$$

The Fourier transform of the normalized longitudinal particle density distribution is called the longitudinal form factor of the bunch:

$$F_{long}(\omega) = \int_{-\infty}^{+\infty} \rho_{long}(t) \exp(-i\omega t)\, dt \tag{35}$$

In Fourier space, the electric field of an extended bunch is obtained by multiplying the electric field of an infinitely short bunch with the longitudinal form factor

$$\tilde{E}_r(\rho, \omega)\, F_{long}(\omega) \tag{36}$$

The form factor has the property that $F_{long}(\omega) \to 1$ for $\omega \to 0$, or more accurately, $F_{long}(\omega) \approx 1$ for $\omega \ll 2\pi/T$ where T is the time duration of the bunch. This implies that all electrons radiate coherently and the intensity grows proportional to N^2 if the wavelength exceeds the bunch length.

The TR spectral energy density is found by a similar calculation as in Sect. 3.3:

$$\begin{aligned} \frac{d^2U_{bunch}}{d\omega d\Omega} &= \frac{d^2U_{GF}}{d\omega d\Omega} \cdot N^2 \left|F_{long}(\omega)\right|^2 \\ &\quad \cdot \left[\frac{2c}{\omega\, r_b \sin\theta} J_1\left(\frac{\omega\, r_b \sin\theta}{c}\right) - \frac{2c\beta\gamma}{\omega\, r_b} I_1\left(\frac{\omega\, r_b}{c\beta\gamma}\right) T(\theta,\omega)\right]^2 \\ T(\theta,\omega) &= \frac{\omega a}{\beta\gamma c} J_0\left(\frac{\omega a \sin\theta}{c}\right) K_1\left(\frac{\omega a}{c\beta\gamma}\right) + \frac{\omega a}{\beta^2\gamma^2 c \sin\theta} J_1\left(\frac{\omega a \sin\theta}{c}\right) K_0\left(\frac{\omega a}{c\beta\gamma}\right) \end{aligned} \tag{37}$$

This formula is valid in the far-field. We observe that in the limit of a very thin and very short bunch ($r_b \to 0$ and $F_{long}(\omega) \to 1$), this expression reduces to the generalized Ginzburg-Frank equation, applied to a bunch of N electrons, since $J_1(x) \approx x/2$ and $I_1(x) \approx x/2$ for small x. The second, and very important, observation is that the radius of the bunch enters the first term of formula (37) in the form $r_b \sin\theta$ where $\sin\theta \ll 1$. The second term in (37) is small if the TR screen radius is sufficiently large, see Sect. 3.3.4. Therefore, in many practical cases the radial dimension of the bunch will have a much weaker influence on the CTR frequency spectrum than the longitudinal dimension. Nevertheless, it is important to investigate to what extent the finite beam radius will influence the determination of the longitudinal form factor.
In the VUV-FEL linac at DESY, the normalized emittance is $\epsilon_n = 2 \cdot 10^{-6}$ m. The beta function may vary between 0.5 m and 200 m. At $\gamma = 1000$ the transverse beam radius r_b is then in the range from 50 to 1000 μm. The transition radiation energy recorded by a detector can be obtained by numerical integration of Eq. (37) over the solid angle of the detection system. This energy is plotted in Fig. 14 as a function of frequency for two acceptance angles, $\theta_{det} = 100$ mrad and 10 mrad, and for beam radii of 50, 150, 350 and 1000 μm, respectively. It is obvious from the figure that the finite TR screen radius leads to a suppression of the frequencies below 1 THz, especially when a detection system with a small solid angle is chosen. The small acceptance angle $\theta_{det} = 10$ mrad would be useful for the investigation of very high-frequency structures (above 10 THz) on the bunches. However, it is not well suited for the determination of the form factor of the VUV-FEL bunches which should ideally have a Gaussian shape with $\sigma = 50$ fs. The squared form

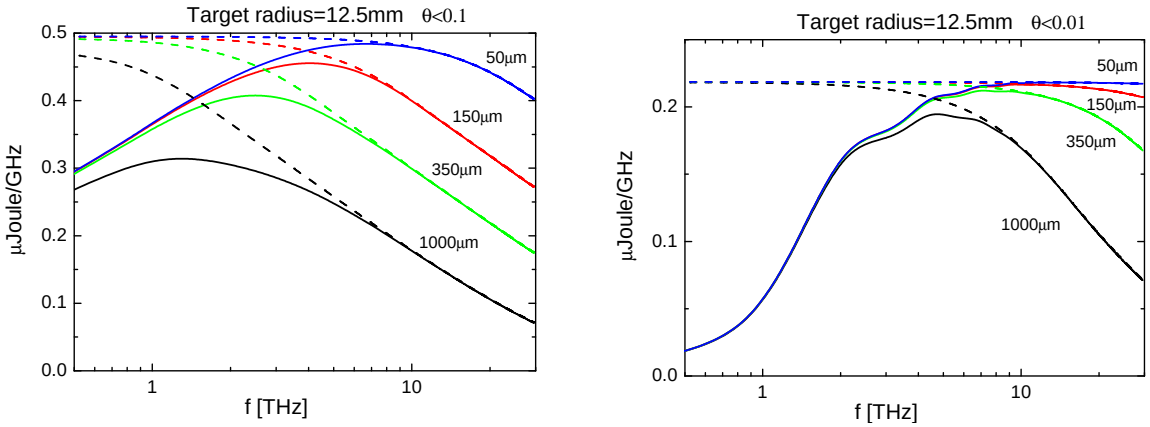

Figure 14: *Far-field coherent transition radiation by an electron bunch with a charge of 1 nC. The detected TR energy in micro-Joule per $\Delta f = 1$ GHz is shown as a function of frequency. The maximum acceptance angle of the detector is $\theta_{det} = 100$ mrad in the left picture and $\theta_{det} = 10$ mrad in the right picture. The solid curves refer to a TR screen radius $a = 12.5$ mm, the dashed curves to an infinitely large TR screen. The bunch radius is varied between 50 and 1000 μm, the bunch length is set to zero.*

factor of such a bunch (see Fig. 15) drops to zero between 1 and 7 THz. In order to get sufficient CTR energy in this range the detection system should have an acceptance angle of 100 mrad or more. Moreover, the electron beam should be well focused to a radius below 150 μm to prevent a distortion of the form factor measurement by the finite beam radius. Figure 15 illustrates that under these conditions the form factor can be easily derived from the measured frequency spectrum of transition radiation.

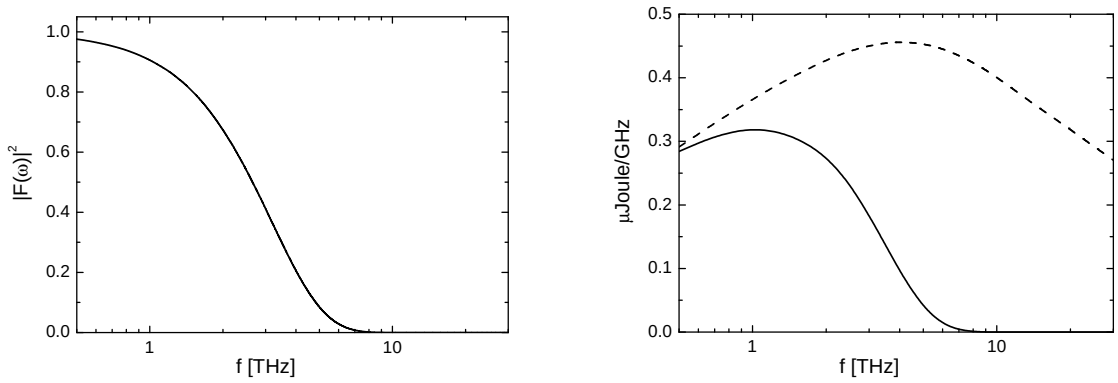

Figure 15: *Left: The squared longitudinal form factor $|F_{long}(\omega)|^2$ for a bunch with a Gaussian longitudinal charge distribution with $\sigma = 50$ fs. Right: Near-field transition radiation emitted by a 1 nC Gaussian bunch with $\sigma = 50$ fs (solid curve). The detector is at a distance of 600 mm from the TR source and has an acceptance angle of $\theta_{det} = 100$ mrad. The bunch radius is $r_b = 150$ μm, the TR screen radius $a = 12.5$ mm. The TR energy emitted by an infinitely short bunch is shown as a dashed curve.*

5 Propagation of Tera-Hertz Radiation by Fourier Transformation

The analytical and semi-analytical computations in Sections 3 and 4 have been based on cylindrical symmetry. This assumption is not justified in many practical cases, for example when one wants to compute transition radiation from asymmetric screens like slit-type diffraction radiators. The numerical two-dimensional Fourier transformation permits us to deal with such situations and offers the additional advantage that the radiation can be propagated through a whole optical system consisting of drift spaces, apertures and focusing elements such as parabolic or elliptic mirrors. Note that the Fourier transform method is restricted to paraxial optics and not applicable for beams with a large angular divergence.

5.1 Computation of diffraction patterns by Fourier transformation

To explain the basic principle of electromagnetic wave propagation by Fourier transformation we generalize Eq. (12) for a TR source screen without cylindrical symmetry. It is then appropriate to work in Cartesian coordinates and choose general points $Q = (\xi, \eta, 0)$ on the source screen and $P = (x, y, D)$ on the observation screen. The two field components at P are

$$\begin{aligned}
\tilde{E}_x(P,\omega) &= -\frac{ik}{2\pi} \underbrace{\int\int}_{TR\ source} \tilde{E}_x(Q,\omega)\, \frac{\exp(ikR')}{R'}\, d\xi d\eta \\
\tilde{E}_y(P,\omega) &= -\frac{ik}{2\pi} \underbrace{\int\int}_{TR\ source} \tilde{E}_y(Q,\omega)\, \frac{\exp(ikR')}{R'}\, d\xi d\eta
\end{aligned}$$

The distance $R' = \overline{QP}$ is expanded up to second order

$$R' = \sqrt{D^2 + (x-\xi)^2 + (y-\eta)^2} \approx D + \frac{x^2+y^2}{2D} - \frac{x\xi + y\eta}{D} + \frac{\xi^2+\eta^2}{2D}$$

We assume here that $(\xi^2+\eta^2) \ll D^2$ and $(x^2+y^2) \ll D^2$. The horizontal component of the Fourier-transformed electric field at an arbitrary point $P = (x, y, D)$ on the observation screen is then given in terms of the horizontal field component on the source screen by the integral:

$$\begin{aligned}
\tilde{E}_x(P,\omega) &= -\frac{ik}{2\pi}\, \frac{\exp(ikD)}{D} \exp\left(\frac{ik(x^2+y^2)}{2D}\right) \\
&\quad \cdot \underbrace{\int\int}_{source} \tilde{E}_x(Q,\omega)\, \exp\left(\frac{ik(\xi^2+\eta^2)}{2D}\right) \exp\left(-i(k_x\xi + k_y\eta)\right)\, d\xi d\eta
\end{aligned}$$

A corresponding expression holds for the vertical field component.

Introducing the "transverse wave numbers"

$$k_x = k\,\frac{x}{D}\,, \quad k_y = k\,\frac{y}{D} \tag{38}$$

with $k = 2\pi/\lambda = \omega/c$ as before, the above integral can be written as a two-dimensional Fourier transformation

$$F_x(k_x, k_y) = \frac{1}{2\pi} \underbrace{\int\int}_{source} G_x(\xi, \eta) \exp[-i(k_x\xi + k_y\eta)]\, d\xi d\eta \tag{39}$$

with the integrand

$$G_x(\xi, \eta) = \tilde{E}_x(\xi, \eta, \omega)\, \exp\left(\frac{ik(\xi^2 + \eta^2)}{2D}\right) \tag{40}$$

For the y component we get correspondingly

$$\begin{aligned} F_y(k_x, k_y) &= \frac{1}{2\pi} \underbrace{\int\int}_{source} G_y(\xi, \eta) \exp[-i(k_x\xi + k_y\eta)]\, d\xi d\eta \\ G_y(\xi, \eta) &= \tilde{E}_y(\xi, \eta, \omega)\, \exp\left(\frac{ik(\xi^2 + \eta^2)}{2D}\right) \end{aligned}$$

The coordinates of the point P are related to the transverse wave numbers by:

$$x = D\,\frac{k_x}{k} \quad y = D\,\frac{k_y}{k}$$

It is important to note that the Fourier integrals can describe both far-field and near-field diffraction since they contain the phase factor $\exp\left(ik(\xi^2 + \eta^2)/(2D)\right)$. As an illustration we look again at the near-field transition radiation at the VUV-FEL which was studied in sect. 3.4.3. Figure 16 demonstrates that the Fourier transform method is in perfect agreement with the semi-analytical computation based on Eq. (25).

The Fourier transform method is quite general and not restricted to the propagation of transition radiation from the TR source to an observation screen. In fact, the method permits the propagation of an arbitrary radiation field through a whole beamline in a stepwise procedure, going from one screen to the next. In each step, the complex electric field vector (amplitude, direction and phase) must be known in a fine grid on the 'source screen'. Using the above algorithm, the complex electric field vector (amplitude, direction and phase) on the 'observation screen' is then computed by FFT, again in a fine grid. In the next step, the previous 'observation screen' is treated as the new 'source screen'. A screen can for example be an aperture, but it may also represent a lens or a focusing mirror of a given size and shape. In that case, position-dependent phase factors are applied to account for the focusing action (see the next section).

5.2 Phase shift by optical elements

The focusing action of lenses and concave mirrors can be incorporated in the framework of the Fourier transform method by means of phase factors which depend on the transverse coordinates. In this section we derive the phase factors for ideal lenses and for spherical, parabolic, ellipsoidal and toroidal mirrors.

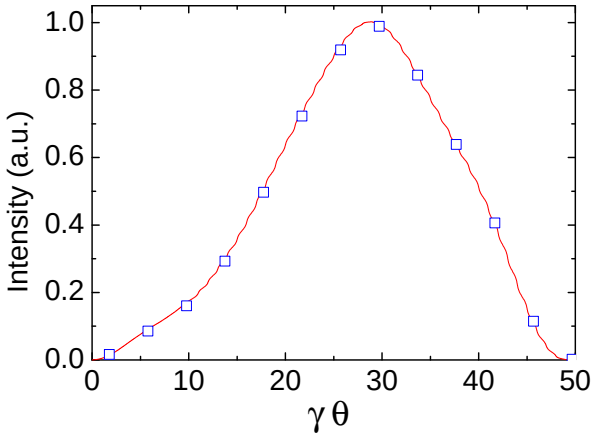

Figure 16: *Angular distribution of transition radiation at the VUV-FEL for the following parameters:* $\lambda = 0.3$ *mm,* $\gamma = 1000$*,* $a = 20$ *mm,* $D = 250$ *mm. Red curve: near-field computation using the second-order Eq. (25). Blue squares: Fourier transform method.*

5.2.1 Ideal lens

We take a thin biconvex lens with a radius of curvature r_c. The focal length is given by

$$\frac{1}{f} = \frac{2(n-1)}{r_c}$$

Call r_0 the radius of the rim of the lens. For a "thin" lens the radius of the rim is much smaller than the radius of curvature, $r_0 \ll r_c$. The thickness of the lens as a function of the radial displacement ξ from the optical axis is given by (see Fig. 17)

$$d(\xi) = 2\left(\sqrt{r_c^2 - \xi^2} - \sqrt{r_c^2 - r_0^2}\right) \approx \frac{r_0^2 - \xi^2}{r_c}$$

for $r_0 \ll r_c$ and $0 \le |\xi| \le r_0$. The wave number in glass is $k' = nk$, so the lens introduces an additional phase advance of the optical wave, as compared to propagation in air

$$\varphi_{lens}(\xi) = (k' - k)d(\xi) = k(n-1)d(\xi) = k\frac{n-1}{r_c}(r_0^2 - \xi^2) = \frac{kr_0^2}{2f} - \frac{k\xi^2}{2f}$$

Hence the phase shift caused by the lens is

$$\varphi_{lens}(\xi) = \frac{kr_0^2}{2f} - \frac{k\xi^2}{2f} \tag{41}$$

To illustrate the importance of this notion we consider the focusing of a parallel light beam. The geometric path length difference between the central path C and an arbitrary parallel path A is

$$L_A - L_C = \sqrt{f^2 + \xi^2} - f \approx \xi^2/(2f) \quad \text{for} \quad \xi \ll f$$

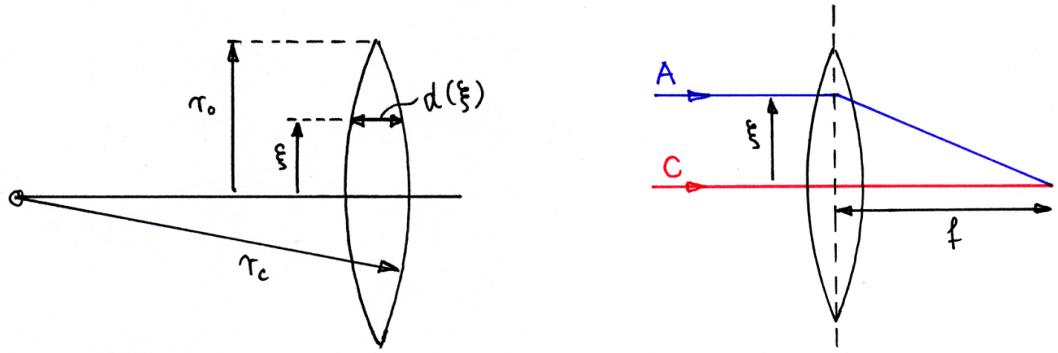

Figure 17: *Left: The thicknes $d(\xi)$ of a biconvex lens as a function of the displacement ξ from the axis. Right: Focusing of a parallel beam by a thin lens. C: central ray, A: arbitrary parallel ray. The reference plane is indicated by the dashed line.*

The same overall phase will be accumulated along all possible paths if the phase shift of the lens (41) is taken into account:

$$\varphi_C + \varphi_{lens}(0) = \varphi_A + \varphi_{lens}(\xi),$$

where $\varphi_A - \varphi_C = k(L_A - L_C)$. We note that φ_{lens} just compensates the geometric path length difference so that all paths acquire the same optical path length. The action of a thin lens on a light ray can be described by a kick angle at the reference plane that is proportional to the displacement from the optical axis.
The focusing by a thin lens can be described by multiplication of the Fourier components with the phase factor

$$\exp(i\varphi_{lens}) = \exp\left(\frac{ikr_0^2}{2f} - \frac{ik\xi^2}{2f}\right) \tag{42}$$

The constant phase $\varphi_0 = kr_0^2/(2f)$ appears in all possible paths and can be omitted.

5.2.2 Parabolic mirror

The principle that the light rays are deflected at the center plane of the lens can be transferred to concave mirrors. We look first at back-reflection. For a plane mirror the situation is simple: the center ray C and any other ray A are simply reversed. Now consider a focusing mirror which has rotational symmetry around the z axis. We request that all incident rays that are parallel to the z axis should be reflected in such a way that they go through the focal point. As our deflecting plane Σ_{def} we choose the plane $z = 0$ that is tangential to the mirror at the center point $(x, y, z) = (0, 0, 0)$. Then, as in the case of the lens, the central ray travels a distance $L_C = f$ from Σ_{def} to the focal point $F = (0, 0, f)$. An arbitrary parallel ray A which is displaced by $\Delta x = \xi$ would travel a distance $L_A = \sqrt{f^2 + \xi^2}$ between Σ_{def} and F, see Fig. 18. In case of the lens the geometric path length difference is compensated by the different distances traveled in glass. Here we must compensate the path length difference by moving the mirror surface away from the deflection plane Σ_{def} by a suitable amount. Let us describe the contour of

the focusing mirror by the equation (here projected into the xz plane)

$$z = g(x)$$

and determine the function $g(x)$. At $x = \xi$ the mirror surface is at a distance $z = g(\xi)$ from the deflection plane $z = 0$. This distance counts twice, so in order to compensate for the path length difference between A and C we request (for small displacements, $\xi \ll f$)

$$L_A - L_C = 2g(\xi) \quad \Rightarrow \quad g(\xi) = (\sqrt{f^2 + \xi^2} - f)/2 \approx \xi^2/(4f)$$

This defines the contour of the focusing mirror, it is a parabola. In three dimensions we get a rotational paraboloid

$$z = g(x, y) = \frac{x^2 + y^2}{2p} \quad \text{with} \quad p = 2f$$

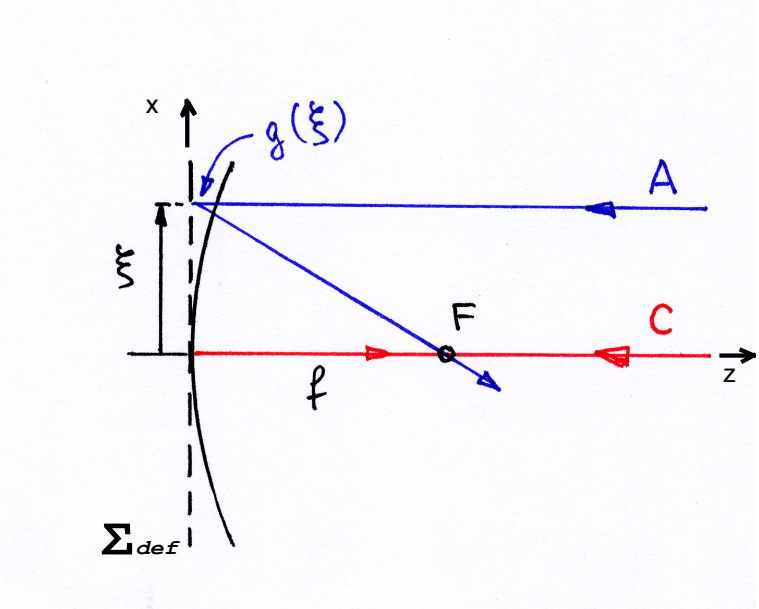

Figure 18: *The focusing of parallel rays by a parabolic mirror. C: central ray, A: arbitrary parallel ray. The deflecting plane Σ_{def} is indicated by the dashed line.*

The parabolic mirror introduces a phase shift that depends quadratically on the distance between the path and the optical axis

$$\varphi_{par} = -\frac{k\xi^2}{2f} \tag{43}$$

5.2.3 Phase shifts introduced by focusing mirrors with 90° deflection

Focusing mirrors with a 90° deflection of the light beam have different properties than mirrors in the back reflection arrangement, see Appendix B.1. The phase shifts for various

types of focusing mirrors with 90° deflection are derived in Appendix B.2. Here we summarize the results. The nomenclature is such that ξ is the distance between the central ray and a parallel ray, measured in the 90° deflection plane, and η is the corresponding distance in the orthogonal plane. For a paraxial beam, the phase shifts are:

Parabolic mirror, incident direction towards focus:

$$\varphi_{par1} = -k\,\frac{\xi^2+\eta^2}{2f} \tag{44}$$

Parabolic mirror, incident direction away from focus:

$$\begin{aligned}\varphi_{par2} &= k\left(-f-\xi+\sqrt{f^2-\eta^2+2f\xi}\right) \\ &\approx k\left(-\frac{\xi^2+\eta^2}{2\,f}+\frac{\eta^2\,\xi}{2\,f^2}+\frac{\xi^3}{2\,f^2}-\frac{3\,\eta^2\,\xi^2}{4\,f^3}-\frac{\eta^4}{8\,f^3}-\frac{5\,\xi^4}{8\,f^3}+O(\xi,\eta)^5\right)\end{aligned} \tag{45}$$

Ellipsoidal mirror:

$$\begin{aligned}\varphi_{ellip} &= -k\,\frac{2}{3}\left(2f+\xi-\sqrt{4f^2-3\eta^2+4f\xi-2\xi^2}\right) \\ &\approx k\left(-\frac{\xi^2+\eta^2}{2\,f}+\frac{\eta^2\,\xi}{4\,f^2}+\frac{\xi^3}{4\,f^2}-\frac{5\,\eta^2\,\xi^2}{16\,f^3}-\frac{3\,\eta^4}{32\,f^3}-\frac{7\,\xi^4}{32\,f^3}+O(\xi,\eta)^5\right)\end{aligned} \tag{46}$$

Toroidal mirror:

$$\begin{aligned}\varphi_{tor} &= k\left(-2f-\xi+\sqrt{-\eta^2-\xi^2+2\sqrt{2}f\left(\sqrt{2f^2-\eta^2}+\sqrt{2}\xi\right)}\right) \\ &\approx k\left(-\frac{\xi^2+\eta^2}{2\,f}+\frac{\eta^2\,\xi}{4\,f^2}+\frac{\xi^3}{4\,f^2}-\frac{\eta^2\,\xi^2}{4\,f^3}-\frac{3\,\eta^4}{32\,f^3}-\frac{3\,\xi^4}{16\,f^3}+O(\xi,\eta)^5\right)\end{aligned} \tag{47}$$

In the Mathematica code *THzTransport* [4] the exact square-root expressions are used.

The focusing quality of the four types of mirrors can be jugded from Fig. 19 where a Gaussian THz beam is incident on the mirror and the intensity distribution in the focal plane is plotted. As expected from the above equations, the parabolic mirror with the incident beam direction towards the focus produces the smallest image.

To check the overall optical quality of the four types of focusing mirrors we have computed with *THzTransport* the optical image of an object that is placed at a distance of $2f_m$ in front of a mirror of focal length f_m. The radiation wavelength is chosen as $\lambda = 0.3$ mm (1 THz). The computed images are shown in Fig. 20 for a focal length of $f_m = 200$ mm and in Fig. 21 for $f_m = 600$ mm. Again the parabolic mirror with the incident beam direction towards the focus generates the best image but at larger focal length the other mirrors produce also acceptable images.

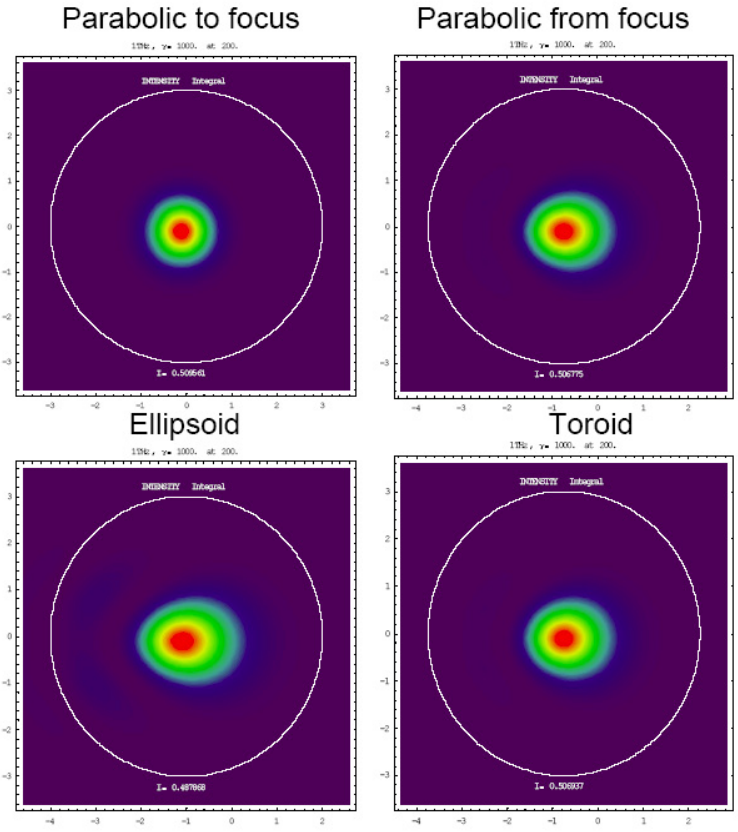

Figure 19: *Intensity distribution in the focal plane for mirrors with* $90°$ *deflection. The incident beam is a Gaussian beam with* $\lambda = 0.3$ *mm.*

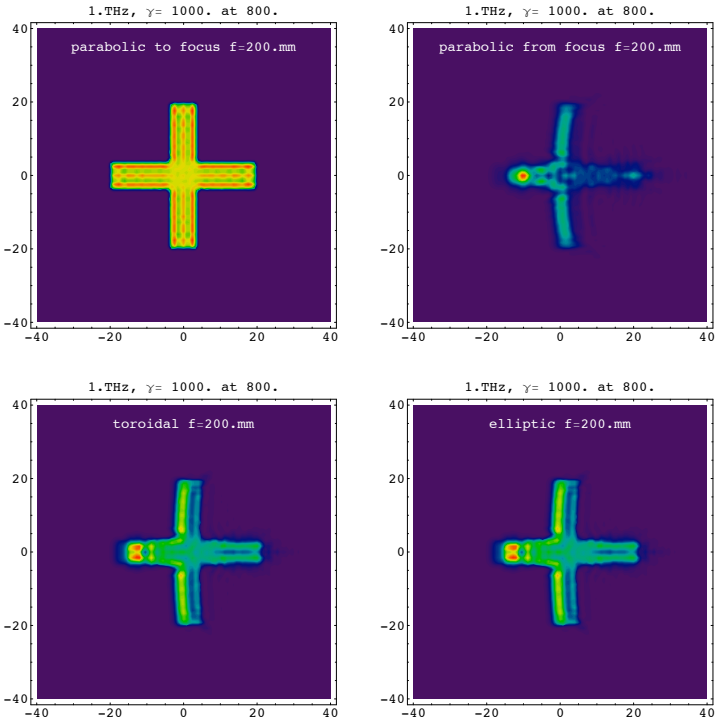

Figure 20: *Computed image of a cross of 40 mm width and height for the four types of focusing mirrors (1:1 imaging). The focal length is 200 mm, the wavelength of the radiation 0.3 mm.*

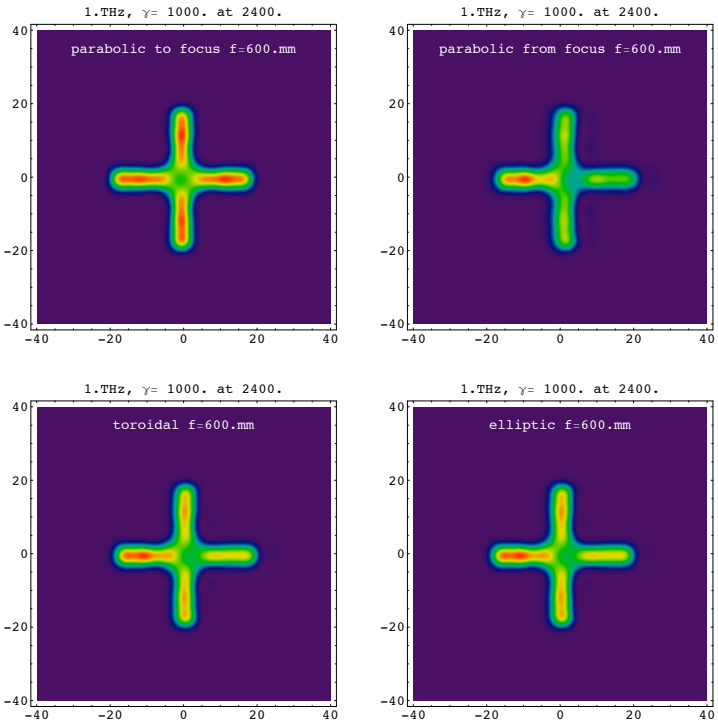

Figure 21: *Computed image of a cross for focusing mirrors with 600 mm focal length.*

Appendix A: Field of a Relativistic Charged Particle

A.1 Derivation by Lorentz transformation

Consider a particle of charge q moving with the constant velocity v along the z direction. In the rest system (t', x', y', z') of the particle one has a pure Coulomb potential and the vector potential vanishes

$$\Phi' = \frac{q}{4\pi\varepsilon_0 r'} \;, \quad \boldsymbol{A}' = 0 \quad \Rightarrow \quad A'^{\mu} = (\Phi'/c, 0) \;. \tag{48}$$

The four-potential $A'^{\mu} = (\Phi'/c, \boldsymbol{A}')$ transforms like a four-vector. Hence the potential in the laboratory system (t, x, y, z) is obtained by the following Lorentz transformation

$$\begin{aligned} \Phi &= \gamma(\Phi' + \beta c A'_z) = \gamma\Phi' \\ A_x &= A'_x = 0 \\ A_y &= A'_y = 0 \\ A_z &= \gamma(A'_z + \beta\Phi'/c) = \gamma\Phi'/c \end{aligned} \tag{49}$$

We have to express the scalar and vector potential as a function of the laboratory coordinates. Using

$$r'^2 = x'^2 + y'^2 + z'^2 = x^2 + y^2 + \gamma^2(z - vt)^2$$

we get

$$\begin{aligned} \Phi(\boldsymbol{r}, t) &= \frac{q}{4\pi\varepsilon_0} \frac{\gamma}{\sqrt{x^2 + y^2 + \gamma^2(z - vt)^2}} \\ \boldsymbol{A}(\boldsymbol{r}, t) &= \frac{\boldsymbol{v}}{c^2}\,\Phi \end{aligned} \tag{50}$$

The electric field in the laboratory system is

$$\boldsymbol{E} = -\nabla\Phi - \frac{\partial \boldsymbol{A}}{\partial t}$$

The components of $\boldsymbol{E}$ are

$$\begin{aligned} E_x &= -\frac{\partial\Phi}{\partial x} = \gamma \cdot \frac{q}{4\pi\varepsilon_0} \cdot \frac{x}{(x^2 + y^2 + \gamma^2(z - vt)^2)^{3/2}} \\ E_y &= -\frac{\partial\Phi}{\partial y} = \gamma \cdot \frac{q}{4\pi\varepsilon_0} \cdot \frac{y}{(x^2 + y^2 + \gamma^2(z - vt)^2)^{3/2}} \\ E_z &= -\frac{\partial\Phi}{\partial z} - \frac{\partial A_z}{\partial t} = \gamma \cdot \frac{q}{4\pi\varepsilon_0} \cdot \frac{z - vt}{(x^2 + y^2 + \gamma^2(z - vt)^2)^{3/2}} \end{aligned} \tag{51}$$

At time $t = 0$ we can write the field in the following vector form

$$\boldsymbol{E}(\boldsymbol{r}) = \frac{q}{4\pi\varepsilon_0} \cdot \frac{(1 - \beta^2)}{(1 - \beta^2 \sin^2\theta)^{3/2}} \cdot \frac{\boldsymbol{r}}{r^3} \tag{52}$$

where $\boldsymbol{r}$ is the radius vector from the charged particle to the observer and θ the angle between $\boldsymbol{r}$ and the velocity vector $\boldsymbol{v}$ of the particle.

The magnetic field is given by the simple expression

$$\boldsymbol{B} = \frac{\boldsymbol{v} \times \boldsymbol{E}}{c^2} \;. \tag{53}$$

A.2 Fourier transformation of the electric field

From now on we use cylindrical coordinates (r, ϕ, z) with $r = \sqrt{x^2 + y^2}$ and $\phi = \arctan(y/x)$ and rewrite the radial field component

$$E_r(r, z, t) = \gamma \frac{q}{4\pi\varepsilon_0} \frac{r}{(r^2 + \gamma^2(z - \beta ct)^2)^{3/2}} \tag{54}$$

Now we make a Fourier transformation of the radial electric field at the position of the TR screen ($z = 0$)

$$\begin{aligned} E_r(r, 0, t) &= \frac{1}{\sqrt{2\pi}} \int_{-\infty}^{\infty} \tilde{E}_r(r, \omega) \exp(i\omega t) d\omega \\ \tilde{E}_r(r, \omega) &= \frac{1}{\sqrt{2\pi}} \int_{-\infty}^{\infty} E_r(r, 0, t) \exp(-i\omega t) dt \ . \end{aligned} \tag{55}$$

The Fourier transform is found to be [5]:

$$\tilde{E}_r(r, \omega) = \frac{q\omega}{(2\pi)^{3/2}\varepsilon_0\beta^2\gamma c^2} K_1\left(\frac{\omega}{\beta\gamma c} r\right) \tag{56}$$

The function K_1 is a modified Bessel function. The longitudinal field component is smaller than the radial component by the factor $1/\gamma$ and can be neglected for highly relativistic electrons. From $\boldsymbol{B} = (\boldsymbol{v} \times \boldsymbol{E})/c^2$ follows that the magnetic field has only an azimuthal component

$$\tilde{B}_\phi = \frac{q\omega}{(2\pi)^{3/2}\varepsilon_0\beta\gamma c^3} K_1\left(\frac{\omega}{\beta\gamma c} r\right) \tag{57}$$

For $x \to 0$ the Bessel function $K_1(x)$ behaves as

$$K_1(x) \approx 1/x \ . \tag{58}$$

A.3 Derivation of the field from the Maxwell equations

Solution of the Maxwell equations for a relativistic point charge

The electric and magnetic fields of a charge traveling along the axis of a cylindrical beam pipe obey the Maxwell equations in vacuum with additional boundary conditions. Assuming cylindrical symmetry for the charge distribution only the radial and longitudinal component of the electric field and the azimuthal component of the magnetic field exist and are independent of the azimuthal angle ϕ. The first Maxwell equation reads

$$\boldsymbol{\nabla} \cdot \boldsymbol{E} = \frac{1}{r}\frac{\partial(rE_r)}{\partial r} + \frac{\partial(E_z)}{\partial z} = \frac{\rho}{\varepsilon_0} \tag{59}$$

while the third and fourth equation

$$\boldsymbol{\nabla} \times \boldsymbol{E} = -\frac{\partial \boldsymbol{B}}{\partial t}, \quad \boldsymbol{\nabla} \times \boldsymbol{B} = \mu_0 \boldsymbol{j} + \frac{1}{c^2}\frac{\partial \boldsymbol{E}}{\partial t}$$

yield

$$\begin{aligned}
\frac{\partial E_r}{\partial z} - \frac{\partial E_z}{\partial r} &= -\frac{\partial B_\phi}{\partial t} \\
-\frac{\partial B_\phi}{\partial z} &= \frac{1}{c^2}\frac{\partial E_r}{\partial t} \\
\frac{1}{r}\frac{\partial (rB_\phi)}{\partial r} &= \mu_0 j_z + \frac{1}{c^2}\frac{\partial E_z}{\partial t}
\end{aligned}$$

The fields travel together with the charge at the speed $v = \beta c$ and depend on the radial coordinate r, the longitudinal coordinate $\zeta = z - \beta ct$ but, due to our assumption of cylindrical symmetry, not on the azimuthal angle. Making a Fourier transformation with respect to ζ we get

$$E_r(r,\zeta) = \frac{1}{\sqrt{2\pi}} \int_{-\infty}^{\infty} \tilde{E}_r(r,k) \exp(ik\zeta) dk$$

with similar expressions for E_z, B_ϕ and the charge density ρ. The wave number is related to the angular frequency by $k = \omega/(\beta c)$. The Fourier components obey the equations

$$\begin{aligned}
\frac{1}{r}\frac{\partial (r\tilde{E}_r)}{\partial r} + ik\tilde{E}_z &= \frac{\tilde{\rho}}{\varepsilon_0} \\
ik\tilde{E}_r - \frac{\partial \tilde{E}_z}{\partial r} &= ik\beta c\tilde{B}_\phi \\
-ik\tilde{B}_\phi &= -ik\frac{\beta}{c}\tilde{E}_r \\
\frac{1}{r}\frac{\partial (r\tilde{B}_\phi)}{\partial r} &= \mu_0 \tilde{j}_z - \frac{ik\beta}{c}\tilde{E}_z
\end{aligned}$$

Combining the second and third equation yields a relation between $\tilde{E}_z$ and $\tilde{E}_r$

$$\frac{\partial \tilde{E}_z}{\partial r} = \frac{ik}{\gamma^2}\tilde{E}_r \tag{60}$$

Inserting this into the first equation we get

$$\frac{\partial^2 \tilde{E}_z}{\partial r^2} + \frac{1}{r}\frac{\partial \tilde{E}_z}{\partial r} - \frac{k^2}{\gamma^2}\tilde{E}_z = \frac{ik\tilde{\rho}}{\gamma^2 \varepsilon_0} \tag{61}$$

The two independent solutions of the homogeneous part of the differential equation (61) are the modified Bessel functions $I_0(kr/\gamma)$ and $K_0(kr/\gamma)$. Due to Eq. (60) the radial field component is then given by the Bessel functions $I_1(kr/\gamma)$ and $K_1(kr/\gamma)$. We know that the field of a relativistic point charge q has to decrease with increasing radius. Hence it will be described by the functions $K_0(kr/\gamma)$ resp. $K_1(kr/\gamma)$ only. Solving the inhomogeneous equation (61) and using Eq. (60) we obtain

$$\tilde{E}_z(r,k) = \frac{-iq\,k}{(2\pi)^{3/2}\varepsilon_0 \beta\gamma^2 c} K_0\left(\frac{k}{\gamma}r\right) \tag{62}$$

$$\tilde{E}_r(r,k) = \frac{q\,k}{(2\pi)^{3/2}\varepsilon_0 \beta\gamma c} K_1\left(\frac{k}{\gamma}r\right) \tag{63}$$

Putting in $k = \omega/v = \omega/(\beta c)$ we see that the second equation agrees with Eq. (56) which was derived by Lorentz-transforming the Coulomb field of the point charge.

Influence of beam pipe

In comparison with the Lorentz-transformation method the differential-equation approach allows to study more complicated cases. A first example is the influence of the metallic beam pipe on the field of the relativistic charge. With the pipe present, the general solution for $\tilde{E}_z$ is a linear combination of $K_0(kr/\gamma)$ and $I_0(kr/\gamma)$ and for $\tilde{E}_r$ a combination of $K_1(kr/\gamma)$ and $I_1(kr/\gamma)$. Assuming a perfectly conducting pipe of radius r_{pipe} the longitudinal field has to vanish at $r = r_{pipe}$. This yields

$$\tilde{E}_z(r,k) = \frac{iq\,k}{(2\pi)^{3/2}\varepsilon_0\beta\gamma^2 c}\left[-K_0\left(\frac{k}{\gamma}\,r\right) + \frac{K_0\left(\frac{k}{\gamma}\,r_{pipe}\right)}{I_0\left(\frac{k}{\gamma}\,r_{pipe}\right)}\,I_0\left(\frac{k}{\gamma}\,r\right)\right] \tag{64}$$

$$\tilde{E}_r(r,k) = \frac{q\,k}{(2\pi)^{3/2}\varepsilon_0\beta\gamma c}\left[K_1\left(\frac{k}{\gamma}\,r\right) + \frac{K_0\left(\frac{k}{\gamma}\,r_{pipe}\right)}{I_0\left(\frac{k}{\gamma}\,r_{pipe}\right)}\,I_1\left(\frac{k}{\gamma}\,r\right)\right] \tag{65}$$

The change of the radial field caused by the beam pipe is generally quite small. In Fig. 22 we show the r-dependence of radial field component, multiplied with r to remove the divergence at $r \to 0$, both without and with the modification by the beam pipe. Only in the vicinity $r \approx r_{pipe}$ one can see a slight increase in field that is caused by the pipe. In most cases the influence of the beam pipe can be neglected in the computation of the

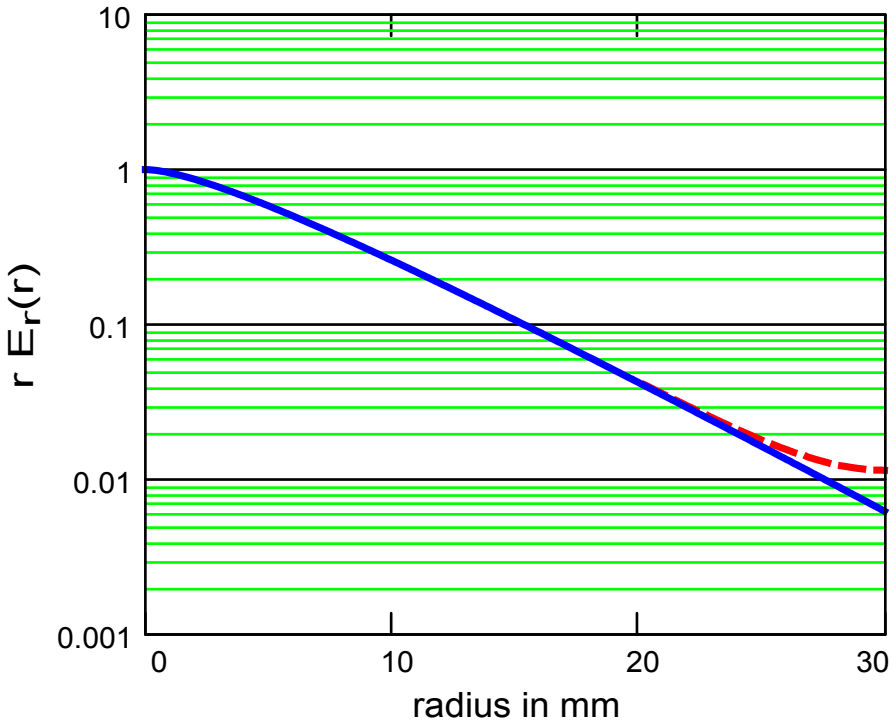

Figure 22: *Radial electric field, multiplied with r, plotted as a function of the radial distance r from the axis. Continuous curve: no beam pipe present, dashed curve: with modification by beam pipe. Parameters: $\gamma = 1000$, $f = 10$ THz, pipe radius $r_{pipe} = 30$ mm.*

transition radiation.

Extended beam

To describe the field of a particle bunch of charge q and finite radius r_b, it is convenient to solve the inhomogeneous equation (61) first for a ring-like charge distribution. Assuming a uniform charge density in the bunch, the charge in a ring of radius $r_{ring} < r_b$ and thickness dr_{ring} is $dq_{ring} = 2q\, r_{ring}\, dr_{ring}/r_b^2$. One obtains for the radial field of the ring charge [6]

$$d\tilde{E}_r(r,k) = \frac{2q\, r_{ring}\, dr_{ring}\, k}{(2\pi)^{3/2} c\varepsilon_0 \beta\gamma r_b^2} \cdot \begin{cases} -K_0\left(\frac{k}{\gamma}\, r_{ring}\right) I_1\left(\frac{k}{\gamma}\, r\right) & \text{for} \quad r < r_{ring} \\ I_0\left(\frac{k}{\gamma}\, r_{ring}\right) K_1\left(\frac{k}{\gamma}\, r\right) & \text{for} \quad r > r_{ring} \end{cases} \tag{66}$$

Integration over the ring radius from zero to the bunch radius r_b yields the field of an extended beam with uniform charge density:

$$\tilde{E}_r(r,k) = \frac{2q}{(2\pi)^{3/2} c\beta\varepsilon_0 r_b} \cdot \begin{cases} K_1\left(\frac{k}{\gamma}\, r_b\right) I_1\left(\frac{k}{\gamma}\, r\right) & \text{for} \quad r < r_b \\ I_1\left(\frac{k}{\gamma}\, r_b\right) K_1\left(\frac{k}{\gamma}\, r\right) & \text{for} \quad r > r_b \end{cases} \tag{67}$$

Here $q = -Ne$ is the total charge of the electron bunch. The finite bunch length has been neglected here. It can be taken into account by multiplying Eq. (67) with the longitudinal form factor $F_{long}(k)$, the Fourier transform of the normalized longitudinal charge distribution.

Appendix B: Focusing Mirrors with 90° Deflection

The focusing of large-bandwidth THz radiation should not be done with lenses because almost all refractive materials exhibit reflection losses at the surfaces and strong frequency-dependent absorption. Focusing metal mirrors with gold plating are the best solution. In a beam line based on mirrors it is often advantageous to have a 90° reflection at each mirror. This precludes the use of a spherical mirror since its focal length in the 90° reflection plane is a factor of two larger than the focal length in the orthogonal plane. Three type of mirrors are suitable: the off-axis paraboloid, the rotational ellipsoid and the toroid.

B.1 Geometric optics of focusing mirrors

Spherical mirror with 90° deflection

An interesting observation is that concave mirrors with a 90° deflection of the light generally have different focusing properties than in the back-reflection arrangement. We illustrate this in Fig. 23 for a spherical mirror with radius R. The mirror has the unfortunate property that the focal length in the 90° deflection plane is $f_1 = R/(2\sqrt{2})$ while the focal length in the orthogonal plane is twice as big. Therefore a spherical mirror in the 90° deflection arrangement is not suitable for the point-focusing of a parallel beam.

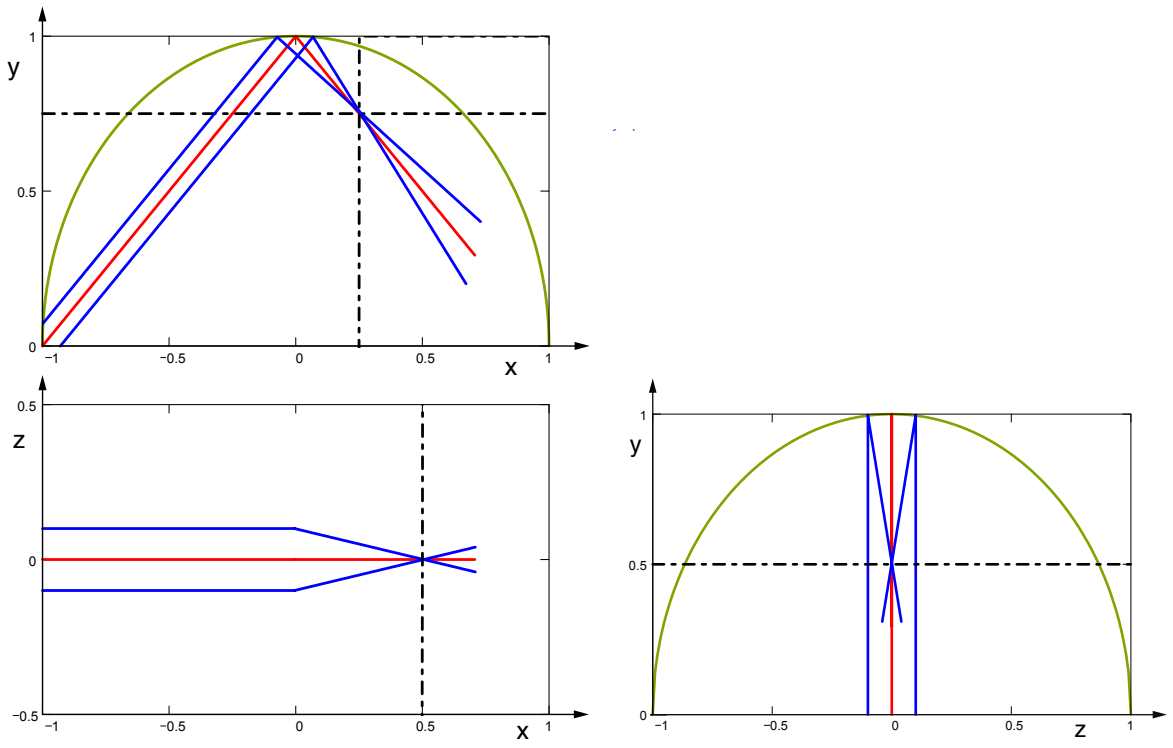

Figure 23: *Focusing of parallel rays by a spherical mirror of radius $R = 1$ with 90° deflection in the (xy) plane. Top left: View of 90° deflection plane, x axis horizontal, y axis vertical. The central ray is plotted in red, the two parallel rays are blue. The focal point is at the intersection of the two dashed-dotted lines. The focal length in the 90° deflection plane is $f_1 = R/(2\sqrt{2})$. Bottom: Focusing of parallel rays (blue) which are displaced in the z direction against the central ray (red). Left: xz plane, x axis horizontal, z axis vertical. Right: zy plane, z axis horizontal, y axis vertical. From these pictures one can see that the focal length in the orthogonal plane is $f_2 = R/(\sqrt{2}) = 2\, f_1$.*

Toroidal mirror

The observations made in Fig. 23 suggest a way out of the dilemma of different focal lengths: the mirror surface must be given a non-isotropic curvature. The radius R_1 in the 90° deflection plane has to be twice as large as the radius R_2 in the orthogonal plane. This leads naturally to a toroidal surface which is obtained by rotating a circle of radius R_2 around an axis that is tangential to the left rim, see Fig. 24.

Ellipsoidal mirror

The rotational ellipsoid with long half axis a and short half axis b has the property that all light rays coming from the left focal point at $-e = -\sqrt{a^2 - b^2}$ are imaged into the right focal point at $+e = \sqrt{a^2 - b^2}$. A 90° reflection is obtained for an eccentricity $e = b$ which implies $a = \sqrt{2}\, b$. The focal length is then

$$f_{ellip} = \sqrt{2}\, b/2 = a/2 \tag{68}$$

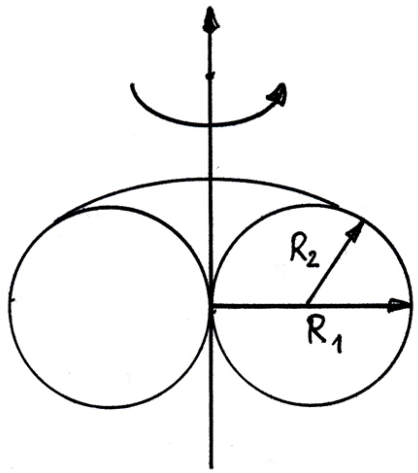

Figure 24: *Generation of a toroidal mirror surface by rotating a circle of radius R_2 around an axis that is tangential to its left rim.*

The point-to-point imaging and the focusing of parallel rays by an ellipsoid with a half-axis ratio of $a/b = \sqrt{2}$ are shown in Fig. 25.

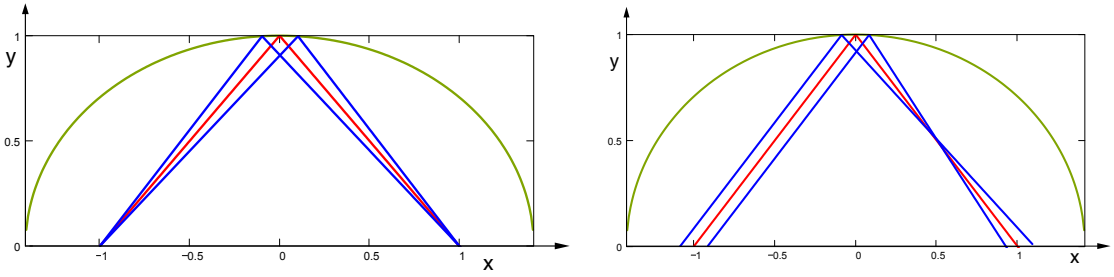

Figure 25: *Left: Point-to-point imaging by a rotational ellipsoid with $b = a/\sqrt{2}$. Right: focusing of parallel rays. The focal length is $f = a/2$. The same focal length is obtained in the orthogonal plane.*

Off-axis paraboloid

Another 90° deflection mirror with point focusing is the rotational paraboloid in the so-called off-axis arrangement. The mirror can be used in two ways, see Fig. 26:
(1) The central light ray C comes in along the negative z direction but is displaced against the symmetry axis by $x = p$. Then all parallel rays are focused in the point $F = (0, 0, p/2)$. The focal length is $f = p$, twice as large as in the back-reflection arrangement.
(2) The central ray starts at the point $(0, 0, p/2)$ and moves in vertical direction. From Fig. 26 one can see that also in this case the focal length is $f = p$.

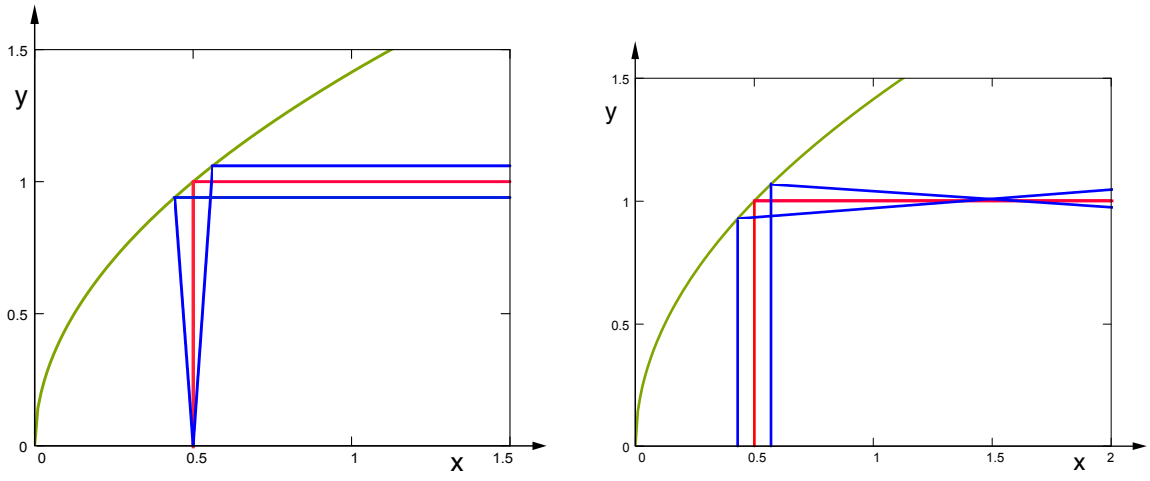

Figure 26: *The off-axis paraboloid with incident direction towards the focus of the parabola (left) and with incident direction away from the focus (right). In both cases the same focal length $f = p$ is obtained in the 90° deflection plane as well as in the orthogonal plane.*

B.2 Phase shifts of focusing mirrors

Within the paraxial approximation the phase shift introduced by a focusing mirror is given by the path length difference between the central path C and an arbitrary parallel path A, $\delta s = L_A - L_C$. In Fig. 27 we show these two paths for the four types of mirrors.

Parabolic mirror, incidence towards focus

For the parabolic mirror with incident direction towards the focus the path difference is $\delta s = L_A - L_C = \xi - \Delta z$. Let us consider two points on the mirror surface: point $P = (f, 0, f/2)$ is on the optical axis of the mirror and point $Q = (f + \xi, -\eta, f/2 + \Delta z)$ is close to P. We want to express Δz as a function of the transverse coordinates ξ, η. To this end we impose that Q is located on the mirror surface, described by the equation $x^2 + y^2 = 2fz$:

$$2f(\frac{f}{2} + \Delta z) = (f + \xi)^2 + \eta^2.$$

From this follows a path length difference and a phase shift given by:

$$\delta s = \xi - \Delta = -\frac{\xi^2 + \eta^2}{2f}, \quad \phi_{par1} = -k\,\frac{\xi^2 + \eta^2}{2f} \tag{69}$$

Hence in the direction towards the focus the parabolic mirror acts as an ideal lens.

Parabolic mirror, direction away from focus

For the parabolic mirror with incident direction away from the focus the path difference is $\delta s = L_A - L_C = \Delta z - \xi$. The point $P = (f/2, 0, f)$ is again at the intersection between the optical axis and the mirror surface, and $Q = (f/2 + \xi, \eta, f + \Delta z)$ is a point close to P. We impose that Q is located on the mirror surface $y^2 + z^2 = 2fx$:

$$f + \Delta z = \sqrt{2f(f/2 + \xi) - \eta^2}.$$

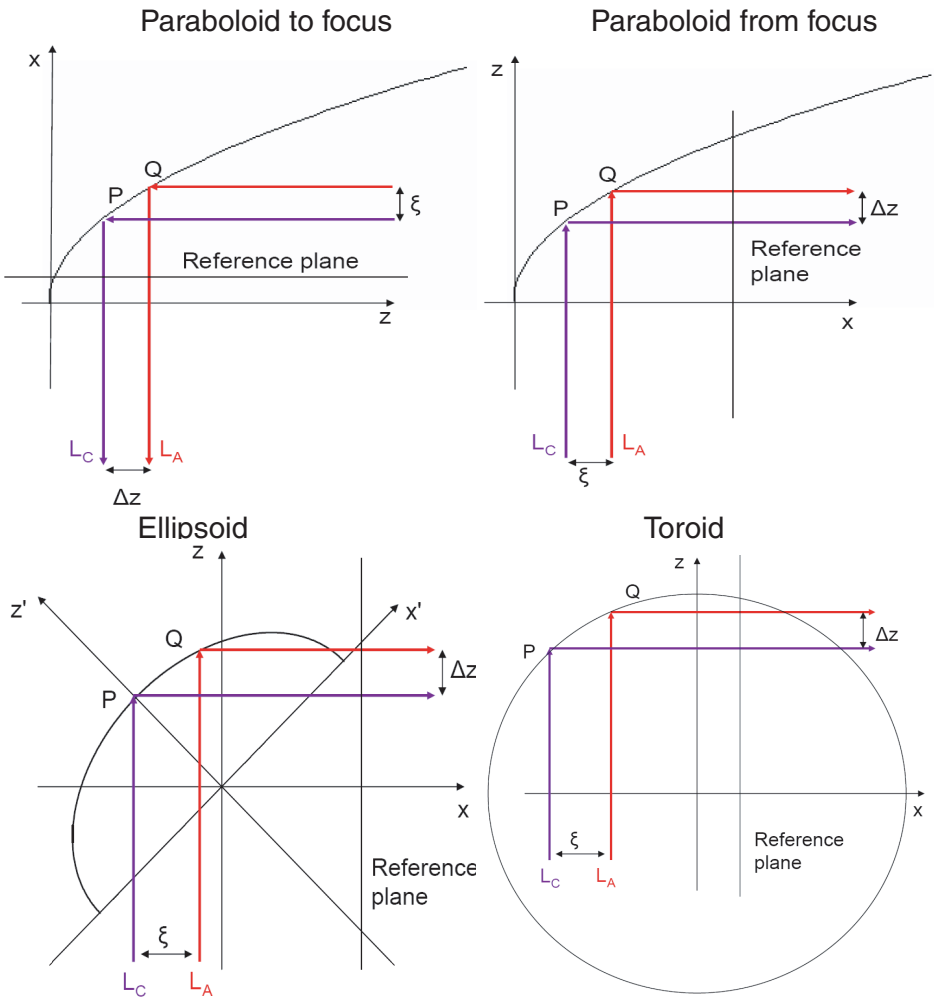

Figure 27: *The four types of focusing mirrors and the definition of the central path, the arbitrary parallel path (displaced by ξ in the xzplane resp. by η in the yz plane). The coordinate system is always defined in such a way that the incident path is along the z direction and the outgoing path along the x direction.*

The path difference is then:

$$\delta s = \Delta z - \xi = -f - \xi + \sqrt{f^2 - \eta^2 + 2f\xi}$$

Ellipsoid

For the ellipsoidal mirror the path difference is $\delta s = L_A - L_C = \Delta z - \xi$. We consider the point $P = (-f, 0, f)$ on the optical axis and a point $Q = (\xi - f, \eta, f + \Delta z)$ close to P. The ellipsoid equation in a rotated (x', y', z') coordinate system with the x' axis parallel to the long axis of the ellipsoid reads

$$\frac{x'^2}{4f^2} + \frac{y'^2}{2f^2} + \frac{z'^2}{2f^2} = 1.$$

The ellipsoid equation in the (x, y, z) system shown in Fig. 27 is obtained by rotating the previous equation around the y' axis by 45° ($x' = (x + z)/\sqrt{2};\ y' = y;\ z' = (z - x)/\sqrt{2}$):

$$x^2 + z^2 + \frac{4}{3}y^2 - \frac{2}{3}xz - \frac{8}{3}f^2 = 0\ .$$

Imposing that Q is located on the mirror surface we obtain:

$$f + \Delta z = \frac{1}{3}(\xi - f) + \frac{\sqrt{2}}{3}\sqrt{12f^2 - 4(\xi - f)^2 - 6\eta^2}\ ,$$

and a path difference:

$$\delta s = -\frac{2}{3}\left(2f + \xi - \sqrt{4f^2 - 3\eta^2 + 4f\xi - 2\xi^2}\right)\ .$$

Toroid

For the toroidal mirror the path difference is $\delta s = L_A - L_C = \Delta z - \xi$. We consider the point $P = (-2f, 0, 2f)$ on the optical axis and a point $Q = (\xi - 2f, \eta, 2f + \Delta z)$ close to P. The toroid equation is:

$$\left(\sqrt{2}f - \sqrt{x^2 + z^2}\right)^2 + y^2 = 2f^2$$

so that:

$$z = \sqrt{\left(\sqrt{2}f + \sqrt{2f^2 - y^2}\right)^2 - x^2}\ .$$

We impose that Q is located on the mirror surface:

$$2f + \Delta z = \sqrt{2f^2 + 2\sqrt{2}f\sqrt{2f^2 - y^2} + 2f^2 - \eta^2 - \xi^2 - 4f^2 + 4f\xi}$$

and obtain the path difference:

$$\delta s = -2f - \xi + \sqrt{-\eta^2 - \xi^2 + 2\sqrt{2}f\left(\sqrt{2f^2 - \eta^2} + \sqrt{2}\xi\right)}\ .$$

References

[1] A derivation of the Ginzburg-Frank equation can be found in: L. D. Landau, E. M. Lifshitz, *Electrodynamics of Continuous Media*, Pergamon, New York, 1960.

[2] M. Castellano et al., *Effects of diffraction and target finite size on coherent transition radiation spectra in bunch length measurements*, Nucl. Instr. and Meth. A, **435**, 297 (1999).

[3] D. Sütterlin, Private communication.

[4] Bernhard Schmidt, *THzTransport*,
http://www.desy.de/ schmidtb/THzTransport/THzTransport.m .

[5] Mathematica, WOLFRAM RESEARCH, INC., www.wolfram.com .

[6] M. Geitz, *Investigations of the transverse and longitudinal beam parameters at the TESLA Test Facility Linac*, Universität Hamburg, 1999, DESY-THESIS-1999-033.